

# Using DC Resistivity Ring Array Surveys to Resolve Conductive Structures Around Tunnels or Mine-Workings

Michael A. Mitchell<sup>a,b,\*</sup>, Douglas W. Oldenburg<sup>a</sup>

<sup>a</sup>*Geophysical Inversion Facility (GIF),  
Department of Earth, Ocean and Atmospheric Sciences,  
University of British Columbia,  
2020-2207 Main Mall,  
Vancouver, British Columbia  
Canada, V6T 1Z4*

<sup>b</sup>*U.S. Geological Survey,  
Volcano Science Center,  
California Volcano Observatory,  
350 N. Akron Rd.,  
Moffett Field, CA 94035*

---

## Abstract

In underground environments, conventional DC direct current (DC) resistivity surveys with a single linear array of electrodes produce fundamentally non-unique inversions. These non-uniqueness and model resolution issues stem from limitations placed on the location of transmitters (TXs) and receivers (RXs) by the geometry of existing tunnels and boreholes. Poorly exciting or sampling Poor excitation and/or sampling of the region of interest (ROI) can create artifacts and reduce the resolution of the recovered model.

To address these problems we propose the use of ring arrays—an ensemble of ring arrays, which are created by placing one or more electrodes in each face (sidewalls, floor, and ceiling) of the tunnel to form a ring of electrodes at each along-tunnel location. Using a series of increasingly complex synthetic models, we assess the benefits of ring arrays and show that they can be used to better constrain the location and shape of anomalous bodies around the tunnel.

Although ring arrays significantly improve the resolution of the recovered model, the size of the comprehensive ring array survey increases rapidly with the number of electrodes used. To balance model resolution and survey size, we developed a physics-based survey design methodology. In this methodology, TXs are selected based upon secondary charge accumulations on a test block that is moved through the ROI. Although this survey design methodology does not produce a strictly optimal survey design, it balances model resolution and survey size in a practical and computationally efficient manner.

Since the ring array more accurately estimates the around-tunnel location of tar-

---

\*Corresponding author

Email address: [mamitchell@usgs.gov](mailto:mamitchell@usgs.gov) (Michael A. Mitchell)

gets and ensures that targets on all sides of the tunnel are detected, it is ideally suited to tunnel-based environments. Our results show that only about 6% of the possible TXs and 0.5% of the RXs in the comprehensive ring array survey are needed to retain the improvements in resolution. ~~This allows~~Therefore, economical ring array surveys ~~to can~~ be designed for both reconnaissance and target characterization. Following the inversion of the reconnaissance dataset, additional rings can be added to reduce the inter-ring spacing or off-tunnel boreholes can be added to the region around identified anomalies to increase resolution as required.

*Keywords:* DC resistivity Resistivity (ERT/ERI), 3-D inversion Inversion , Survey Design, In-mine, Tunnel, SimPEG

---

### CRediT authorship contribution statement

**Michael A. Mitchell:** Conceptualization, Methodology, Formal analysis, Investigation, Writing-Original Draft, ~~Writing-Review~~Writing-Review & Editing, Funding Acquisition.

**Douglas W. Oldenburg:** Conceptualization, Methodology, Supervision, ~~Writing-Review~~Writing-Review & Editing, Funding Acquisition.

## <sup>1</sup> 1. Introduction

<sup>2</sup> **DC Direct current (DC)** resistivity surveys, which allow us to image variations in  
<sup>3</sup> the electrical conductivity of the subsurface, can be used in any application where  
<sup>4</sup> there is a conductivity contrast between the target and background. In a DC resis-  
<sup>5</sup> tivity survey a constant current is injected between a pair of current or transmitter  
<sup>6</sup> (TX) electrodes and potential differences are measured between one or more pairs  
<sup>7</sup> of receiver (RX) electrodes. The accumulation of electrical charge on the interface  
<sup>8</sup> between regions of differing electrical conductivities alters the measured potential dif-  
<sup>9</sup> ferences. The observed ~~variations the differences in~~ measured potentials can be used  
<sup>10</sup> to construct a model showing variations in the subsurface distribution of electrical  
<sup>11</sup> conductivity using geophysical inversion. Some applications in which DC resistivity  
<sup>12</sup> surveys are useful include: mapping aquifers, tracking environmental containments in  
<sup>13</sup> groundwater, mineral exploration, geothermal exploration and monitoring, and void  
<sup>14</sup> detection in karst terrain.

<sup>15</sup> Although DC resistivity surveys have been used extensively above ground since  
<sup>16</sup> the 1950s, most studies involving subterranean use have occurred in the last 30 years.  
<sup>17</sup> In one of the earliest applications, Scott et al. (1968) used ~~1D-one-dimensional (1-D)~~1D-one-dimensional (1-D)  
<sup>18</sup> Wenner array soundings along the walls of a tunnel to characterize the competency of  
<sup>19</sup> the rock and measure the thickness of fractured material from blasting. In-mine DC  
<sup>20</sup> resistivity soundings and ~~2D-two-dimensional (2-D)~~2D-two-dimensional (2-D) arrays have been used in Germany  
<sup>21</sup> to estimate the free water content and monitor wet regions within old salt mines which  
<sup>22</sup> are being used for the storage of radioactive waste (Kessels et al., 1985; Yaramancı,  
<sup>23</sup> 2000). For mineral exploration in Japan Sasaki and Matsuo (1990) used a ~~2D-2-D~~2D-2-D  
<sup>24</sup> ERT inversion of surface-to-tunnel and tunnel-to-tunnel DC resistivity data to map  
<sup>25</sup> disseminated copper ore at a mine site and Arai (1995) used a ~~2.5D-D~~2.5D-D ERT inversion

to map the location of a resistive lead-zinc sulphide ore vein within a Japanese mine. Ramirez et al. (1996) showed that ~~3D~~three-dimensional (3-D) ERT can be used to monitor underground storage tanks for leaks. In South Africa, researchers have used tunnel to tunnel ERT surveys to identify potholes, dykes, and iron-rich ultramafic pegmatite (IRUP) bodies that disrupt ore zones in platinum mines (van Schoor, 2005; van Schoor and Binley, 2010). To characterize and monitor small scale rock fracturing due to excavation, Kruschwitz and Yaramanci (2004) and Gibert et al. (2006) used ~~2D~~2-D DC modeling and inversion of a few rings of electrodes placed around the circumference of a tunnel. In Chinese coal mines, a great deal of research has been undertaken to develop DC resistivity techniques to detect water-bearing structures ahead of the cutting machinery (Wang, 2011; Han et al., 2011).

Much of our current research builds upon work done by ~~Maxwell et al. (2005); Eso et al. (2006e,a,b); and Mitchell and Oldenburg (2016b,a)~~ Maxwell et al. (2005), Eso et al. (2006a,b,c), Cisyk et al. (2014), Maxwell and Cisyk (2016) and Mitchell and Oldenburg (2016a,b) at the Mosaic potash mines near Esterhazy, Saskatchewan. Here they conducted several ~~2D and 3D~~2-D and 3-D DC resistivity studies to map regions of wet salt and brine. To improve resolution in their ~~3D surveys~~3-D surveys, off-plane electrodes were placed in raises, sub-drifts, and off-tunnel boreholes to better constrain the location of conductive targets. These studies, along with nearly all of the others listed above, discuss our inability to properly resolve ~~3D structures with 2D~~3-D structures with 2-D arrays or a limited number of off-plane electrodes in ~~3D surveys~~3-D surveys. ~~This highlights 3-D surveys. These challenges highlight~~ the need for further research and refined survey design methodologies for in-mine or tunnel-based environments.

Underground environments, such as tunnels or mine-workings, ~~are challenging environments in which to collect present challenges for~~ DC resistivity data collection due to the limited electrode geometry afforded by the tunnels. Unlike surface applications, where a dense grid of transmitters (TXs) and receivers (RXs) can be deployed to maximize model resolution within the region of interest (ROI), the subterranean environment often limits the location of TXs and RXs to existing tunnels, boreholes, or other workings. ~~This~~These physical limitations on the location of TXs and RXs can significantly reduce model resolution and create non-uniqueness issues when the target region is not properly sampled. ~~Tsourlos et al. (2011) noted similar challenges when using borehole-to-surface arrays.~~

These limitations were highlighted ~~while reading about by~~ previous studies and ~~working through work~~ on two underground DC resistivity field datasets, one from the Mosaic K2 potash mine near Esterhazy, Saskatchewan (Mitchell and Oldenburg, 2016a,b), and the other from the Laboratoire Souterrain à Bas Bruit (LSBB) in Rustrel, Vaucluse, France (Maxwell et al., 2010). To confidently interpret the inversion results, several questions needed to be addressed regarding the resolution of the recovered conductivity models. Two synthetic tunnel models, which mimicked the field examples, were created to investigate these questions. The first is a straight section of tunnel, akin to LSBB, while the second contains a tunnel laid out in an asymmetric horseshoe as in the Mosaic example. While working with these synthetic models the following pitfalls were observed.

When collecting DC data along a straight section of tunnel, conventional surveys

71 used only a single linear array of electrodes placed along one face (sidewall, floor, or  
72 ceiling) of the tunnel. Although a 2D-2-D array of this type can often constrain the  
73 along-tunnel location of a potential target it cannot resolve the target's around-tunnel  
74 location and poorly constrains how far the target is away from the tunnel. Similar  
75 challenges arise with more complex tunnel geometries if most of the transmitters  
76 and receivers fall on or near the same depth plane. In this situation, it is difficult  
77 or impossible to determine where the anomalous bodies are located relative to the  
78 measurement plane.

79 *1.1. Paper Outline*

80 Before proceeding with our investigation of model resolution and non-uniqueness,  
81 we start with a brief overview of forward modeling and inversion (see Section 2).  
82 These numerical processes are fundamental to our analysis since they allow us to  
83 simulate data given a conductivity model and reconstruct a geologically reasonable  
84 estimate of the conductivity model that fits the recorded data. We then proceed to  
85 describe our research.

86 To design a survey which addresses the identified model resolution and non-  
87 uniqueness issues we first need to understand why they occur. In Section 3 we analyze  
88 these shortcomings using a series of simple examples that illustrate the impact of data  
89 detectability and sensitivity on inversion results. To address these model resolution  
90 and non-uniqueness issues, we propose the use of an ensemble of ring-shaped arrays  
91 of electrodes. The ring array is created by placing one or more electrodes in each face  
92 (sidewalls, floor, and ceiling) of the tunnel to form a ring of electrodes at each along-  
93 tunnel location. Using a series of synthetic models, which increase in complexity, we  
94 assess the benefits of these design modifications in Section 4.

95 Since the full ring array survey typically uses four times more electrodes than the  
96 single linear array, for a given along-tunnel electrode spacing, it contains many more  
97 possible measurements and can be costly to collect. This prompted us to develop  
98 a new survey design methodology (see Section 5). In this methodology, TXs are  
99 selected based on secondary charge accumulation on a target test block, which is  
100 moved through the ROI. This metric ensures that a subset of TXs which best excite  
101 the ROI is selected. RXs for each of the selected TXs are then pseudo-randomly  
102 selected from a subset of measurements that are sufficiently sensitive to one or more  
103 of the test block locations. We do not claim that this is a strictly optimal survey  
104 design but show it to be a practical and computationally efficient procedure that  
105 balances improvements in model resolution and survey size.

106 **2. Background Theory**

107 Forward modeling and inversion are important tools for solving geophysical prob-  
108 lems. Forward modeling allows us to compute predicted data given a conductivity  
109 model and inversion is used to reconstruct an estimate of the conductivity model  
110 from our observed data. Forward modeling is an integral part of inversion since it is  
111 used to determine how well the recovered model fits the observed data. The model is  
112 iteratively updated until a geologically reasonable solution is found which adequately

113 fits the observed data. All of the DC forward modeling and inversions presented in  
114 this paper were completed using the open-source python package SimPEG (Cockett  
115 et al., 2015).

116 In the forward problem a ~~3D~~-3-D finite volume discretization on a staggered mesh,  
117 in which  $\sigma$  and  $\phi$  are defined on cell centers, is used solve the following system of  
118 partial differential equations (Haber et al., 2000; Pidlisecky et al., 2007; Cockett et al.,  
119 2015, 2016).

$$\nabla \cdot \sigma \nabla \phi = I(\delta(r - r_{s+}) - \delta(r - r_{s-})) \quad (1)$$

120 ~~Where~~where  $\sigma$  is the electrical conductivity,  $\phi$  is the electric potential, and  $I(\delta(r -$   
121  $r_{s+}) - \delta(r - r_{s-}))$  is the galvanic source term, which is represented by the sum of Delta  
122 Dirac functions centered about the positive and negative source electrode locations  
123  $r_{s+}$  and  $r_{s-}$  scaled by the injection current ( $I$ ). An octree mesh, where the cell  
124 refinement is a function of the electrode locations and conductivity structures, was  
125 used to greatly reduce the number of model cells from that of a standard tensor mesh  
126 (Haber and Heldmann, 2007; Haber et al., 2012a).

127 Since the inverse problem is typically very under-determined ~~,~~(i.e., there are  
128 far more model cells than data), we pose it as a regularized Tikhonov optimization  
129 problem. The inverse problem is solved by finding an estimate of the true model ( $\hat{m}$ ),  
130 which minimizes the model objective function ( $\Phi_m$ ), while driving the data misfit  
131 ( $\Phi_d$ ) to its target level ( $\Phi_d^*$ ). This minimization problem can be formalized in the  
132 following manner.

$$\begin{aligned} \min \Phi &= \Phi_d + \beta \Phi_m \\ \text{s. t. } \Phi_d &\leq \Phi_d^* \end{aligned} \quad (2)$$

133 ~~Where~~where  $\beta$  is a regularization parameter that controls the relative importance of  
134 the model objective function ( $\Phi_m$ ) and the data misfit ( $\Phi_d$ ).

135 The data misfit ( $\Phi_d$ ) provides a quantitative measure of the difference between  
136 predicted data ( $\vec{d}^{pred}$ ), derived through numerical modeling, and the observed data  
137 ( $\vec{d}^{obs}$ ). We defined  $\Phi_d$  as follows.

$$\Phi_d = \sum_{i=0}^n \left( \frac{\vec{d}_i^{pred} - \vec{d}_i^{obs}}{\xi_i} \right)^2 = \|\mathbf{W}_d (\mathbf{d}^{pred} - \mathbf{d}^{obs})\|_2^2 \quad (3)$$

138 ~~Where~~where  $\xi_i$  is the standard deviation of the  $i$ th datum. The data weighting  
139 matrix  $\mathbf{W}_d = \text{diag}[1/\xi_1, \dots, 1/\xi_n]$ . Since the data uncertainties, which are cumula-  
140 tively referred to as the noise model, are typically unknown ~~,~~ they must be estimated  
141 (Oldenburg and Li, 2005).

142 To control the complexity of the recovered model, we used the following formula-  
143 tion for the model objective function ( $\Phi_m$ ).

$$\Phi_m = \|\mathbf{W}_s(\mathbf{m} - \mathbf{m}_{ref})\|_2^2 + \sum_{i=1}^3 \|\mathbf{W}_i \mathbf{m}\|_2^2 \quad (4)$$

144 **Where** the first term controls the “smallness” of the model (i.e., how close the  
145 current model ( $\mathbf{m}$ ) is to the reference model ( $\mathbf{m}_{ref}$ )) and the summation contains  
146 directional derivative terms, which control the smoothness of the model in each direc-  
147 tion.  $\mathbf{W}_s$  is a diagonal matrix containing cell weights while the three components of  
148  $\mathbf{W}_i$  ( $\mathbf{W}_x$ ,  $\mathbf{W}_y$ , and  $\mathbf{W}_z$ ) combine finite difference operators and face weight vectors  
149 in each direction (Oldenburg and Li, 2005).

150 More details regarding our formulation of the forward and inverse problem can be  
151 found in Mitchell and Oldenburg (2016a) and Mitchell (2020). For additional infor-  
152 mation on geophysical inversion, we refer the reader to the following books: Menke  
153 (1984), Parker (1994), Aster et al. (2018), and Haber (2014). Oldenburg and Li (2005)  
154 provide a general overview of geophysical inversion in their tutorial while  
155 Li and Oldenburg (1994), LaBrecque et al. (1996), Loke and Barker (1996), Ramirez  
156 et al. (1996), and Loke et al. (2013) are a few of the many papers which specifically  
157 discuss the inversion of DC resistivity data.

### 158 3. Non-Uniqueness and Model Resolution in Tunnel-Based DC Resistivity 159 Surveys

160 To illustrate some of the model resolution and non-uniqueness issues that are  
161 faced in these subterranean environments, we started with a linear array of electrodes  
162 buried in a fullspace and built up intuition from there. The linear array of electrodes  
163 extended in the positive  $x$ -direction from  $x=0$  m to  $x=50$  m with elec-  
164 trodes spaced every 5 m. Both the analytic response of a sphere in the proximity of  
165 an electrical current point source along with numerical modeling and inversion results  
166 of an equivalent volume cube were used to analyze different electrode configurations.  
167 These tools highlighted the limitations of a single linear array of electrodes and im-  
168 proved our understanding of how electrode geometry impacts model resolution and  
169 non-uniqueness.

#### 170 3.1. Offset TX Electrode Trials

171 Using the equation derived by Wait (1982) the analytic electrical potential due to  
172 a sphere excited by a current point can be computed at any RX location outside of the  
173 sphere. A summary of this derivation can also be found in Mitchell (2020). Starting  
174 with a linear array of electrodes extending in the positive  $x$ -direction we  
175 calculated the pole-pole response of 4 spheres which are centered at (25 m, 8 m, 0 m),  
176 (25 m, 0 m, 8 m), (25 m, -8 m, 0 m), and (25 m, 0 m, -8 m) respectively, respectively,  
177 to a TX located at (25 m, 0 m, 0 m). The radius of the spheres was chosen so that  
178 they would have the same volume as a 5 m cube. A background conductivity of  $5e-3$   
179  $5 \times 10^{-3}$  S/m and a sphere conductivity of 10 S/m were used in keeping with values  
180 from the potash salt mine environment. The geometry of this experiment is shown  
181 in Figure 1 and the resulting potentials are shown in Figure 2. With each trial that  
182 follows, one or more offset TX electrodes are added to the array and the differences in  
183 response are evaluated. Figure 3 shows an example with a single TX electrode offset  
184 in the positive  $z$ -direction.

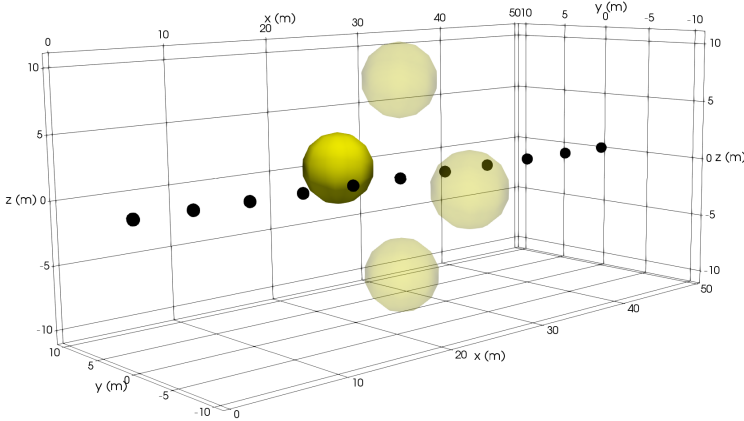


Figure 1: Oblique view of the experimental setup for a linear array of electrodes embedded in a fullspace. The analytic response of a pole-pole survey with the TX electrode at (25 m, 0 m, 0 m) is calculated for 4 separate conductive spheres centered at: (25 m, 8 m, 0 m), (25 m, 0 m, 8 m), (25 m, -8 m, 0 m), and (25 m, 0 m, -8 m), respectively. In this Figure Sphere #1 is solid while the other spheres are translucent.

185 To assess the performance of each survey the problem was discretized on an octree  
 186 mesh with 1 m cubic cells in the core region and a 5 m conductive cube was placed  
 187 at the same center location as sphere 1 (25 m, 8 m, 0 m). Synthetic data ~~was~~ were  
 188 then forward modeled and inverted for each survey. To minimize complicating factors  
 189 and promote the best possible recovery of the conductive block no noise was added  
 190 to the forward modeled data and uncertainties were set using only a small floor value  
 191 of  $1e-6 \times 10^6$  V/A.

### 192 3.1.1. Trial 1: Single Linear Array

193 Due to the symmetry of the single linear array, any sphere of the same radius  
 194 and conductivity that is centered on the dotted circle in Figure 2a will produce an  
 195 identical secondary response, as shown in panel b). Since there is no difference in the  
 196 modeled data, the inversion has no way to constrain the true location of the sphere.

197 The first row of plots in Figure 4 shows how this fundamental non-uniqueness in  
 198 measured potentials translates into the recovered inversion model. While the inversion  
 199 of the single linear array can determine the along array location ( $x$ -location) of the  
 200 anomalous body it was unable to constrain the around array location ( $y$  and  $z$ -  
 201 location) of the conductive cube. In the recovered model the conductive anomaly  
 202 forms a circular ring around the electrode array. Dealing with this non-uniqueness  
 203 requires modification of the survey design to break the symmetry inherent to the  
 204 single linear array.

### 205 3.1.2. Trial 2: Linear Array of RXs with an Electrode Offset in the Y or Z Direction

206 To break the symmetry of the single linear array a single electrode was added  
 207 to the array, which is offset in either the  $y$  or  $z$  direction. Figure 3 shows  
 208 the results of offsetting the TX electrode by 2 m in the positive  $z$  direction.

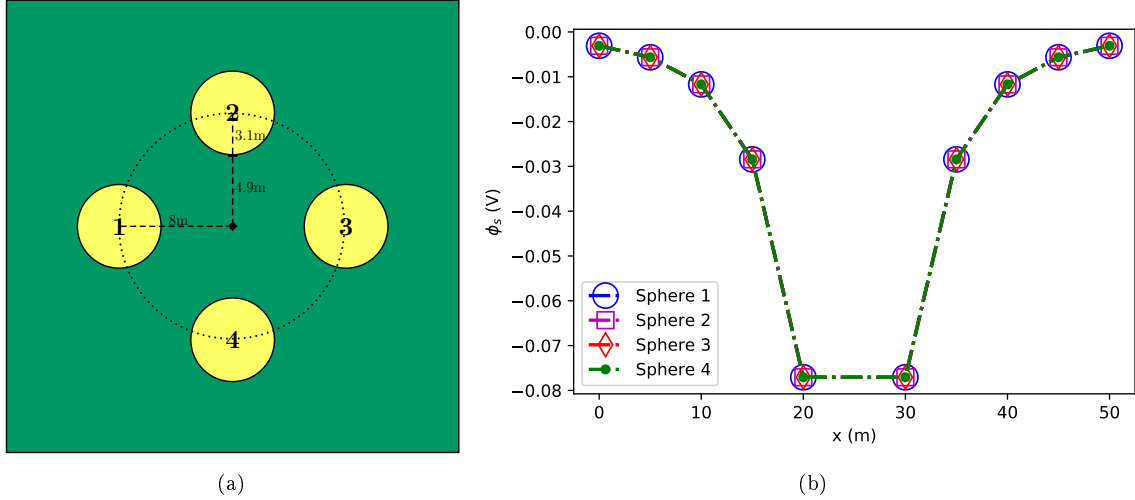


Figure 2: Panel 2a shows the location of the conductive (yellow) spheres laid out symmetrically around the linear array of electrodes (black dots), which extends into and out of the page. Panel 2b shows the secondary potentials at the pole RX locations for each of the 4 spheres. As a result of the symmetry, the measured response of each sphere is identical.

so that it is located at (25m, 0m, 2 m). The pole-pole data profiles in Figure 3b show that the  $z$  offset TX electrode breaks the symmetry of the linear array since the current source is now closer to sphere 2 than sphere 4. This alters the distribution of the secondary currents and charges enough to produce a measurable difference in the response of spheres 2 and 4. However, the responses of spheres 1 and 3 remain identical since these spheres are still symmetrically positioned with respect to the electrodes. Similarly, if the TX electrode is offset by 2 m in the positive  $y$ -direction (25m, 2m, 0 m) spheres 1 and 3 can be differentiated but spheres 2 and 4 cannot.

Using the same mesh and model from Trial 1, data was forward modeled and inverted for these surveys with a single offset TX. Sections from the  $z$  offset TX inversion model are shown in the second row of Figure 4. In this inversion, the conductive anomaly is preferentially placed in close proximity to the offset current electrode above the electrode array instead of its true location to the side of the array. This type of artifact clearly shows that having a measurable difference in the recorded data is a necessary but not sufficient condition for addressing this particular model non-uniqueness problem. In addition to having measurable differences between each of the 4 spheres the distribution of sensitivities also needs to be considered.

The sensitivity ( $J$ ) is a measure of the change in the  $i$ th datum as a result of a unit change in the  $j$ th model cell  $\left(J_{ij} = \frac{\partial d_i}{\partial m_j}\right)$ . Since measurements are more sensitive to conductivity changes in close proximity to the electrode locations, the inversion preferentially adds structure in these high sensitivity regions to reduce the data misfit ( $\phi_d$ ) while minimizing the smallness term of the model objective function ( $\phi_m$ ). McGillivray and Oldenburg (1990) and Spitzer (1998) further discuss theoretical aspects of sensitivity and the main ways to compute it.

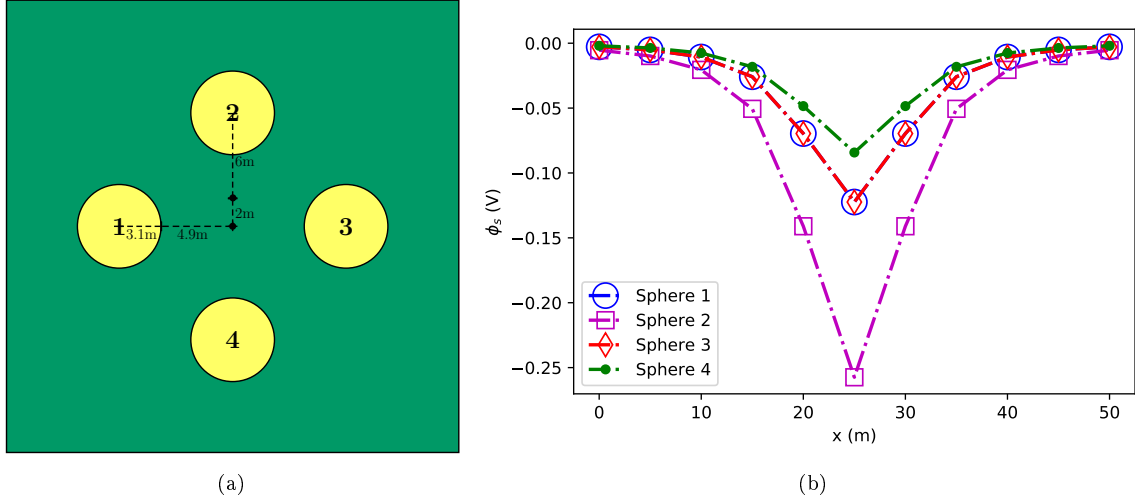


Figure 3: Panel 3a shows the location of the conductive (yellow) spheres laid out symmetrically around the linear array of RX electrodes, which extends into and out of the page. An additional electrode, which is offset by 2 m in the ~~+z direction~~ positive  $z$ -direction, has been inserted at (25m, 0m, 2 m) for the TX electrode. Panel 3b shows the secondary potentials at the pole RX locations for each of the 4 spheres. The  $z$  offset of the TX electrode allows us to differentiate the response of spheres 2 and 4. The response of spheres 1 and 3 remain identical, however, since they are symmetrically positioned relative to the electrodes.

### 234 3.1.3. Trial 3: Linear Array of RX with 2 Orthogonal Offset Electrodes

235 To slowly build up the complexity of the survey, one of the  $y$  and  $z$  single offset  
 236 TX datasets are now combined. The combined survey has 2 TXs and 20 data. Since  
 237 Trial 2 showed that the data from the  $y$  offset TX can differentiate sphere/block 1  
 238 and 3 and the data from the  $z$  offset TX can differentiate sphere/block 2 and 4 the  
 239 combined dataset should have the ability to differentiate the responses of conductive  
 240 anomalies in any of these locations. The inversion results of a  ~~$-y$ - $y$~~  and  $+z$  offset  
 241 TX dataset are shown in the third row of Figure 4. This result shows that if neither  
 242 of the electrodes is offset in the same direction as the conductive block, then the  
 243 recovered conductive anomaly is centered about the closer TX and is smeared out  
 244 ~~towards~~ toward the true location of the conductive block. This misleading inversion  
 245 result once again appears to be a result of asymmetric sensitivity bias. When there is  
 246 a transmitter near the conductive block, the measured secondary potentials are larger  
 247 and sensitivity bias appears to have a smaller impact on the recovered model.

### 248 3.1.4. Trial 4: Linear Array of RX with 4 Orthogonal Offset Electrodes

249 Two more offset TX datasets were then added to form a survey with 4 orthogonal  
 250 offset TX electrodes. The resulting survey contained 4 TXs and 40 data. This  
 251 survey was then tested to see if the symmetric distribution of sensitivities would  
 252 help minimize the artifacts and smearing that were observed in the inversion results  
 253 of previous trials. The fourth row of Figure 4 shows section views of the greatly  
 254 improved inversion model. In this recovered model the location of the conductive  
 255 block to the north of the electrode array is unambiguously identified and there is no

256 visible smearing of the conductive anomaly around the electrode array.

257 *3.2. Tunnel Effects*

258 After considering the symmetry related non-uniqueness issues discussed illustrated  
259 by Trials 1-4, a simple experiment akin to the 4 sphere trials was designed to show  
260 how the presence of a tunnel impacts the ability of a linear array of electrodes to  
261 constrain the around-tunnel location of a conductive body. In this experiment, a  $3 \times$   
262  $3$  m tunnel is centered about the origin and extends along  $x$ -axis in the positive and  
263 negative directions. As in the previous trials, a linear array of electrodes is used with  
264 electrodes placed every 5 m from  $x = 0$  m to  $x = 50$  m in the ceiling of the tunnel. A  
265 pole TX is placed in the center of the array, at a location of (25m, 0m, 2 m) and the  
266 remaining 10 electrode locations are used as pole RXs. Four separate conductivity  
267 models were then created, each containing a 5 m conductive (10 S/m) cube centered  
268 8 m away from the electrode array. Blocks 1 to 4 are centered about: (25m, -8m, 2  
269 m), (25m, 0m, 10 m), (25m, 8m, 2 m), and (25m, 0m, -6 m). Figure 5a  
270 shows an amalgamated diagram with the location of all 4 conductive (yellow) blocks  
271 relative to the resistive (blue) tunnel and electrode array (black dots).

272 The much lower secondary response from Block 4, which is on the opposite side  
273 of the tunnel as the TX electrode, is due to the current shielding effects of the  $3 \times$   
274  $3$  m tunnel, which are illustrated by the current density plots in Figure 6. The  
275 tunnel distorts the distribution of primary currents by forcing them to flow around  
276 the resistive tunnel. Primary current densities are greatest above the tunnel and  
277 diminish as they flow around the tunnel. This ~~The tunnel~~ has a shielding effect on  
278 the medium below and to the sides of the tunnel~~and~~, which causes conductive bodies  
279 in these regions to produce smaller secondary responses. Figure 5b summarizes the  
280 measured secondary potentials from each of the 4 conductive blocks. These results  
281 align with our intuition since block 2, which lies above the TX and tunnel, has the  
282 largest amplitude  $\phi_s$ , and  $\phi_s$  values decrease in magnitude as the block is moved  
283 ~~further~~ farther around the tunnel. Since all of the block centers are 8 m away from  
284 the pole TX, any variations in  $\phi_s$  must be solely due to the tunnel.

285 Although, in this configuration, the tunnel has broken the vertical symmetry, hor-  
286 izontal symmetry is retained ~~As as~~ shown by the identical  $\phi_s$  responses of blocks 1  
287 and 3. For any location along the dashed circle there will be a second point mirrored  
288 about the  $y$ -axis that will produce an identical response. This configuration is anal-  
289 ogous to the situation with a single offset TX in Trial 2 with the addition of current  
290 shielding effects.

291 *3.3. Summary of Non-Uniqueness and Resolution Analysis*

292 The results presented in this section show that in addition to having detectable  
293 differences in the data, TXs also need to be laid out symmetrically to create a uniform  
294 distribution of sensitivities about the array. To avoid inversion artifacts similar to  
295 those shown in Figure 4, where conductive anomalies are incorrectly placed in regions  
296 with comparatively high sensitivity, the use of a “ring” of orthogonal electrodes is  
297 required. The shielding effect of the tunnel further accentuates sensitivity imbalances  
298 since the poorly excited regions on the opposite side of the tunnel from the TX have

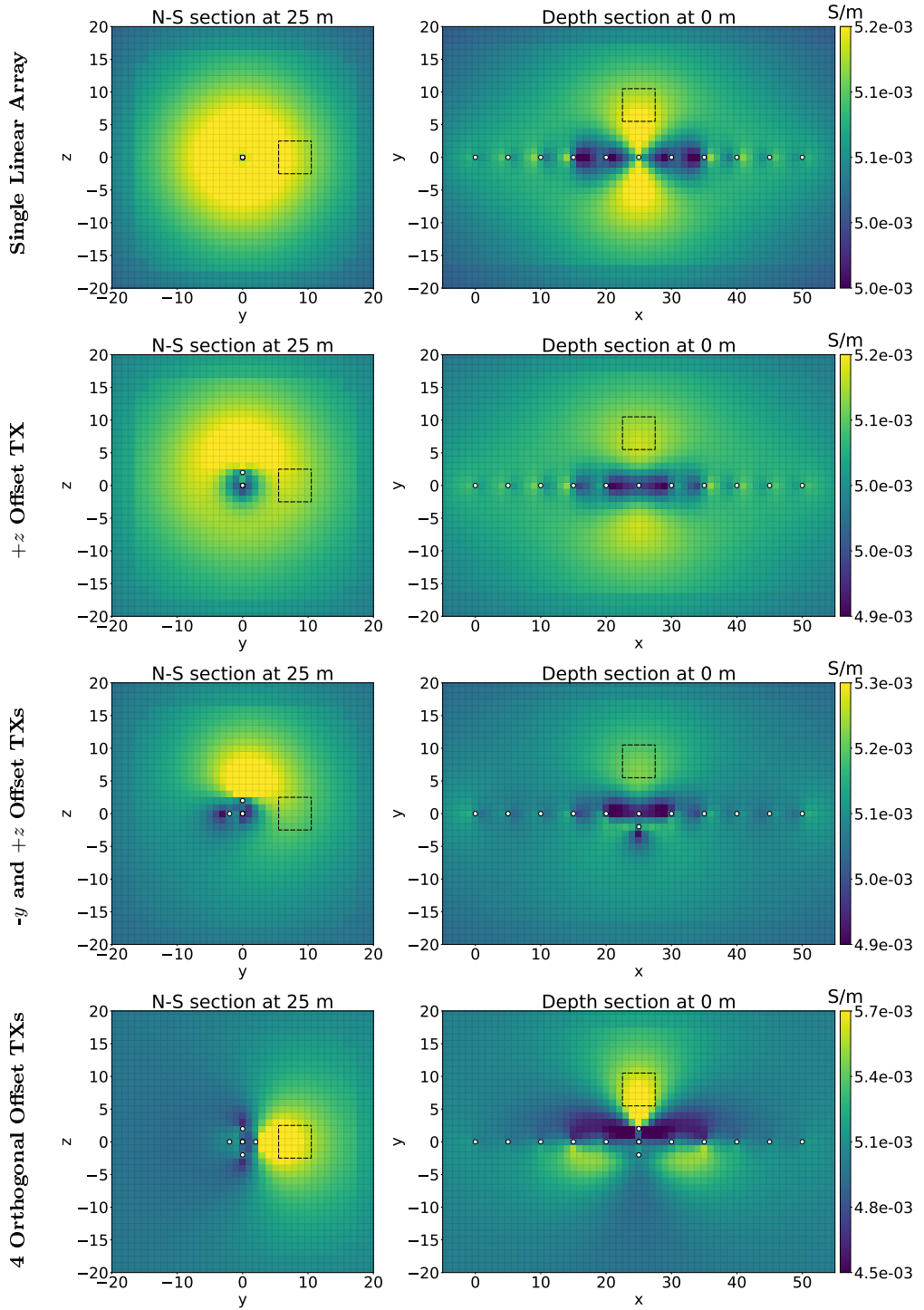


Figure 4: A series of  $x$  and  $z$  sections through the recovered models showing how our ability to constrain the location of a conductive block off to the side of the tunnel changes depending on the use of different offset TXs. The white dots are projections of the electrode locations onto the section and the black dashed outlines show the edges of structures in the true model.

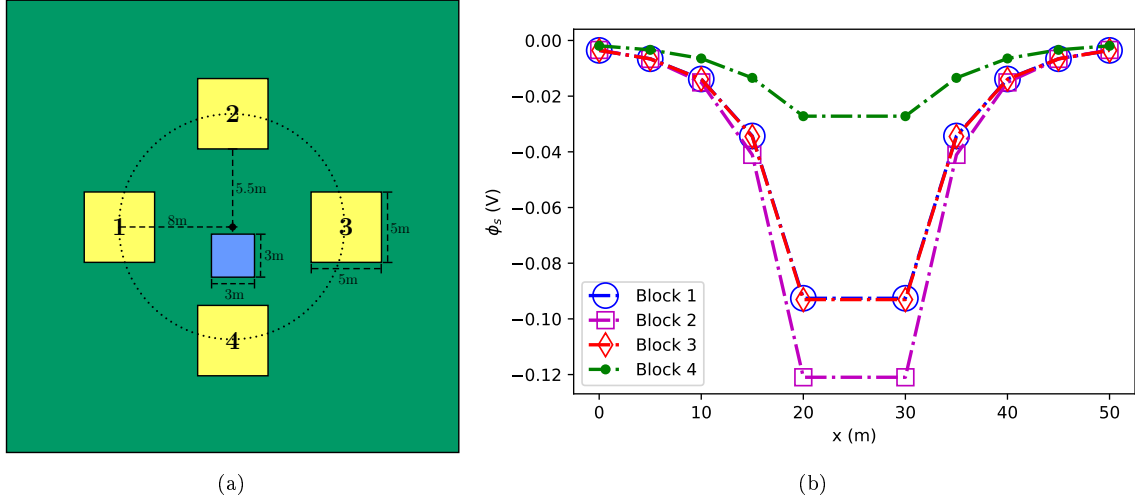


Figure 5: Panel 5a shows the location of the conductive (yellow) 5m cubes laid out symmetrically around the linear array of electrodes (black dot). The electrodes are embedded into the ceiling of the  $3 \times 3$  m air filled, resistive (blue) tunnel. Both the electrode array and tunnel extend into and out of the page. Panel 5b shows the secondary potentials at the pole RX locations for each of the 4 blocks. In this configuration the tunnel breaks the vertical symmetry and allows us to differentiate the response of blocks 2 and 4. Horizontal symmetry is maintained with the single linear array, however, so the secondary response of blocks 1 and 3 are identical.

extremely low sensitivities. By placing one electrode in each face of the tunnel to form a ring of electrodes at each along-tunnel location, we can differentiate the response of conductive bodies at any location around the tunnel and uniformly distribute sensitivities.

#### 4. Developing and Testing the Ring Array Survey

To address the model resolution and non-uniqueness issues discussed in the previous section, we propose the use of ring-shaped arrays of electrodes. Using a series of increasingly complex synthetic models we assess the benefits of ring arrays for designing surveys that better constrain the location and shape of anomalous bodies around the tunnel. Since ring arrays utilize far more electrodes than conventional linear arrays, we developed a physics-based survey design methodology that aids in the selection of a subset of TXs and RXs. In the proposed survey design methodology, TXs are selected based upon charge accumulation on a target test block, which is moved through the region of interest (ROI) and RXs are pseudo-randomly selected from a subset of measurements, which are sufficiently sensitive to the test block. We do not claim that this is a strictly optimal survey design, but show it to be a practical and computationally efficient way to balance improvements in model resolution with survey size.

##### 4.1. Selection of Base Survey Parameters

Before testing the ring array, appropriate base survey parameters need to be selected to ensure that anomalous bodies within the ROI are detectable. To perform

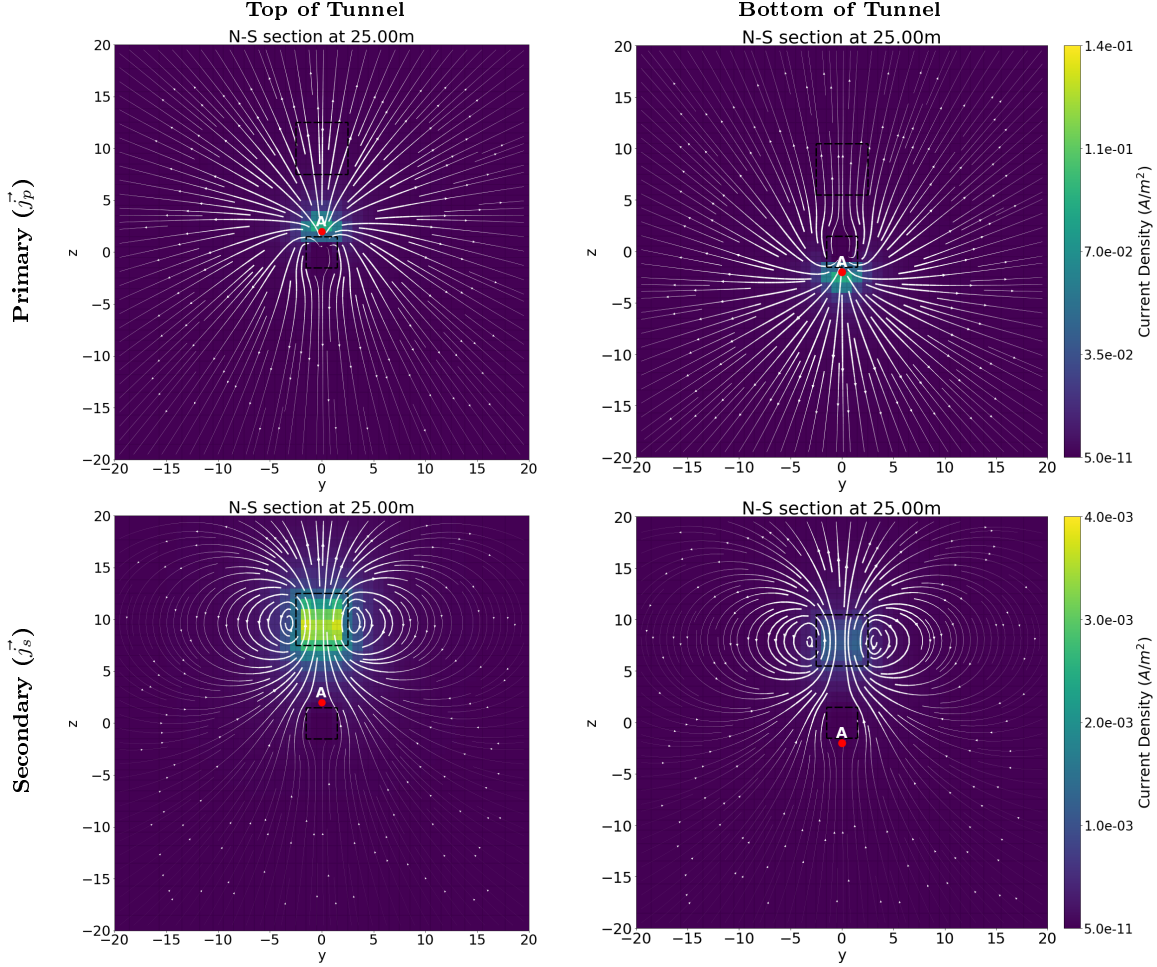


Figure 6: N-S sections showing variations in the primary and secondary current densities as the location of the pole TX (red dot) is moved to various sides of the  $3 \times 3$  m tunnel. In the left column, the TX is on the tunnel ceiling and in the right column, the TX is on the floor of the tunnel. As in previous figures, the dashed black lines show the outlines of the conductive block and the E-W trending tunnel. The white arrows show current flow lines. As the TX is moved ~~further~~<sup>farther</sup> around the tunnel, the primary current density in the vicinity of the conductive block decreases and the TX does a poorer job of exciting the target. In this way, the tunnel effectively shields the conductive block from the TX and reduces the magnitude of its secondary response.

320 this analysis we need to define the ROI, estimate the size of the target, and estimate  
321 the conductivity contrast between the target and background. With these estimates,  
322 forward modeling can be done to measure the response of different targets and de-  
323 termine which will be detectable. For a more detailed ~~—~~discussion on detectability  
324 estimates see Mitchell (2020).

325 After some analysis of different array types, we determined that dipole-dipole mea-  
326 surements were best suited for this application since they had the highest near-tunnel  
327 sensitivities. Spitzer (1998), Dahlin and Zhou (2004), and Okpoli (2013) ~~provide~~  
328 provided a good review of sensitivity variations and the resolution capacity of com-  
329 monly used arrays. ~~It should be noted that~~ Here we use the term dipole-dipole gener-  
330 ally to refer to any electrode configuration which utilizes a pair of electrodes for both  
331 the TX and RX. As a result, the comprehensive set of dipole-dipole configurations  
332 that are tested here incorporate all possible 4 electrode combinations and therefore  
333 include Wenner, Schlumberger, traditional dipole-dipole, gradient, and  $\gamma$ -array style  
334 measurements. All of these 4 electrode array types are found to have higher sensi-  
335 tivity and better resolution than pole-pole arrays (Dahlin and Zhou, 2004; Okpoli,  
336 2013). By combining measurements from each of these 4 electrode array types we  
337 make use of the strengths of each individual array type to balance horizontal and  
338 vertical sensitivity to variations in conductivity and maximize resolution.

339 Selecting appropriate electrode separation distances is also important. For ~~3D~~  
340 3-D surveys, having evenly spaced electrodes in each direction has been shown to  
341 improve the overall resolution of the recovered model (Okpoli, 2013). In the case of  
342 the ring array, this suggests that the along-tunnel or inter-ring separation distance  
343 should not be dramatically larger than the intra-ring spacing of electrodes. Since  
344 electrodes were placed in the center of each face of the  $3 \times 3$  m tunnel at a distance  
345 of 2 m from the tunnel center, these synthetic trials have an intra-ring electrode  
346 spacing of 2.83 m. The electrodes were sunk half a cell into the tunnel wall to ensure  
347 that they are grounded and minimize numerical errors. An inter-ring spacing of 5 m  
348 along the length of the tunnel was found to produce far better inversion results than  
349 a 10 m inter-ring spacing. Figure 7 illustrates the difference between intra-ring and  
350 inter-ring electrode separations. When the inter-ring spacing is considerably larger  
351 than the intra-ring spacing it creates an imbalanced distribution of sensitivities, with  
352 much higher sensitivities around the tunnel at the ring locations than between the  
353 rings. This situation dramatically reduces the overall resolution of the survey and  
354 can cause inversion artifacts to be placed near the electrode rings or smeared from  
355 ring to ring.

356 When selecting inter-ring and intra-ring electrode separation distances it is also  
357 important to take into account the estimated size of your target and the expected  
358 distance of the target from the tunnel/electrodes. A good rule of thumb is to select  
359 inter-ring and intra-ring electrode spacings similar to the larger of these two estimates.  
360 Since the sensitivity, and therefore the resolution of the array, decays rapidly ~~as you~~  
361 ~~move~~ away from the electrodes there is no reason to collect measurements using a  
362 very small electrode spacing if you expect the target to be far from the tunnel. These  
363 closely spaced measurements will help better constrain the near-tunnel region but  
364 will do little to improve the resolution of the distant target region. Conversely, trying

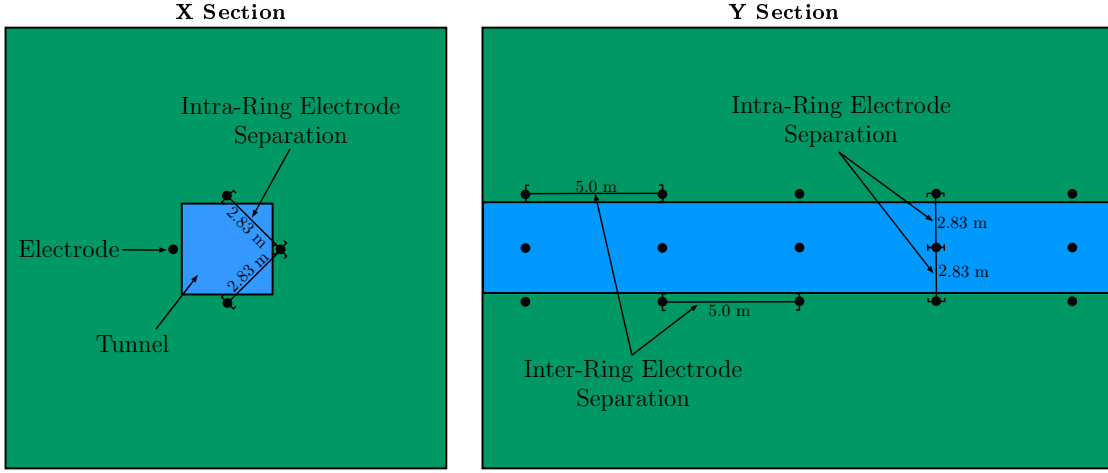


Figure 7: Diagrams illustrating the difference between inter-ring and intra-ring electrode separation distances. Intra-ring separations measure the distance between electrodes within a single ring and inter-ring separations specify the distance between rings. The left column shows a N-S oriented section which perpendicularly cuts the tunnel, while the right column shows an E-W oriented section that parallels the tunnel. Electrode locations are marked by the black dots around the periphery of the blue  $3 \times 3$  m tunnel.

365 to resolve a small target close to the tunnel with a large electrode spacing reduces  
 366 sensitivity and resolution within the region of interest and can result in a missing or  
 367 highly smeared anomaly in the recovered model.

#### 368 4.1.1. Straight Tunnel Synthetics

369 The performance of the ring array was first tested on a series of models with  
 370 conductive structures placed at various locations around a straight section of  $3 \times 3$  m  
 371 tunnel. In keeping with the previous modeling, a background conductivity of  $5e-3$   
 372  $5 \times 10^{-3}$  S/m and a block conductivity of 10 S/m were used. With these models, we  
 373 assess the ring arrays' ability to constrain the around-tunnel location of the target, the  
 374 distance of the target away from the tunnel, and its ability to resolve more complex  
 375 structures that mimic geology.

376 For each of these tests, we start simple and build up the complexity of the survey.  
 377 Results are shown for a single linear array, 4 linear ~~arrays~~array, and the ring array  
 378 surveys. Diagrams showing orthogonal views of each survey layout are shown in  
 379 Figure 8. In these diagrams, the dashed lines denote the boundaries of the ROI  
 380 which extends from  $x = 15$  m to  $x = 35$  m and from -20 m to 20 m in the  $y$   
 381 and  $z$ -directions, respectively.

382 For the single linear array electrodes were placed at 5 m intervals from  $x = 0$  m  
 383 to 50 m along the ceiling of the tunnel. In the 4 linear array survey, one of these  
 384 11 electrode linear arrays is laid along the center of each tunnel face. For each of  
 385 the linear arrays, data are collected independently (i.e., all TX and RX electrodes  
 386 were on the same face of the tunnel), but inverted collectively. For the ring array  
 387 survey, rings of 4 electrodes with 1 electrode in the center of each face of the tunnel  
 388 are placed at 5 m intervals within the central ROI and 10 m intervals outside of the  
 389 ROI. For each of these surveys, all possible 4 electrode dipole-dipole measurements

390 were included to form a comprehensive dataset. This caused the size of the survey to  
 391 increase rapidly as the number of electrodes increased. Table 1 summarizes the size  
 392 of each of these surveys.

	# Electrodes	# TX	# Data
Single Linear Array	11	55	1,980
Four Linear Arrays	44	220	7,920
Ring Array	36	630	353,430

Table 1: A table showing the size of each of the surveys tested in terms of the number of electrodes used, the number of TXs, and the total number of data.

#### 393 4.1.2. Around-Tunnel Location of the Target

394 To characterize the ability of each survey to constrain the around-tunnel location  
 395 of the target, we placed a 5 m conductive cube 3 m away from the southern wall of the  
 396 tunnel. As in previous examples, the conductive block has a conductivity of 10 S/m  
 397 and the background conductivity is  $5e-3 \times 10^{-3}$  S/m. Using SimPEG, synthetic  
 398 data was forward modeled for each survey, contaminated with 2% Gaussian  
 399 noise (i.e., randomly sampled noise from a normal distribution which varies from 0  
 400 to 2% of each measurement), and inverted. The results of these inversions show that  
 401 our ability to constrain the around-tunnel location of the conductive block improves  
 402 substantially as the survey is built up from the single linear array to the ring array  
 403 (see Figure 9).

404 Although the single linear array helps determine the along-tunnel location of the  
 405 block, it does a very poor job of constraining its around-tunnel location. The re-  
 406 covered anomaly forms a conductive ring centered about the electrodes in the center  
 407 of the tunnel ceiling, instead of its true location on the southern side of the tunnel.  
 408 This conductive ring-like artifact is a result of the single linear array's inherent non-  
 409 uniqueness in constraining the around-tunnel location of anomalies as discussed in  
 410 Section 3 and its highly asymmetric distribution of sensitivities. With the 4 linear  
 411 array survey, the recovered anomaly is now located on the correct side of the tunnel  
 412 and is spherical, but underestimates the distance of the block from the tunnel. The  
 413 recovered model continues to improve with the introduction of the ring array. The  
 414 conductive anomaly has now pulled away from the tunnel and moved closer to its true  
 415 location on the south side of the tunnel. With the ring array, the recovered anomaly  
 416 is also more compact and has a higher conductivity contrast with the background.

#### 417 4.1.3. Resolving Multiple Blocks

418 We then increased the complexity of the model by adding several conductive blocks  
 419 at various locations around the tunnel. Figure 10 shows two 3D views of the true  
 420 multiple block model with the blocks labeled 1-3 for ease of reference. In keeping with  
 421 the previous trials, the blocks were assigned a conductivity of 10 S/m in contrast to  
 422 the  $5e-3 \times 10^{-3}$  S/m background.

423 Figure 11 shows the inversion models from each of the array types tested. Since  
 424 the blocks all lie in different planes, it is difficult to display the results using model

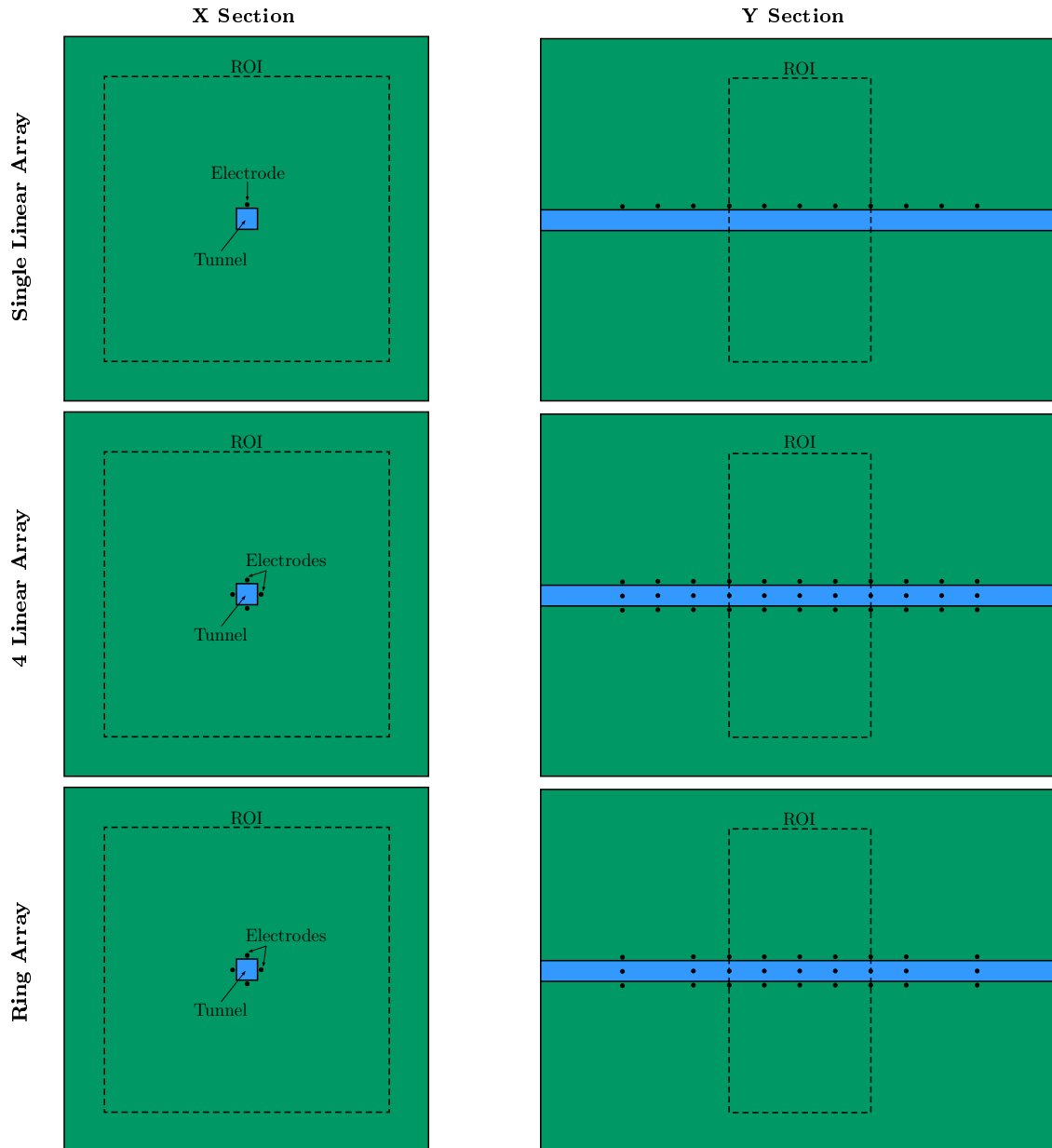


Figure 8: A series of diagrams showing orthogonal views of each survey layout. The left column shows N-S oriented sections which perpendicularly cut the tunnel, while the right column shows E-W oriented sections that parallel the tunnel. Each row of figures shows the changes in electrode placement as the complexity of the survey increases from the single linear array (top) to the ring array survey (bottom). The dashed lines mark the boundaries of the region of interest (ROI) around the tunnel. Electrode locations are marked by the black dots around the tunnel periphery.

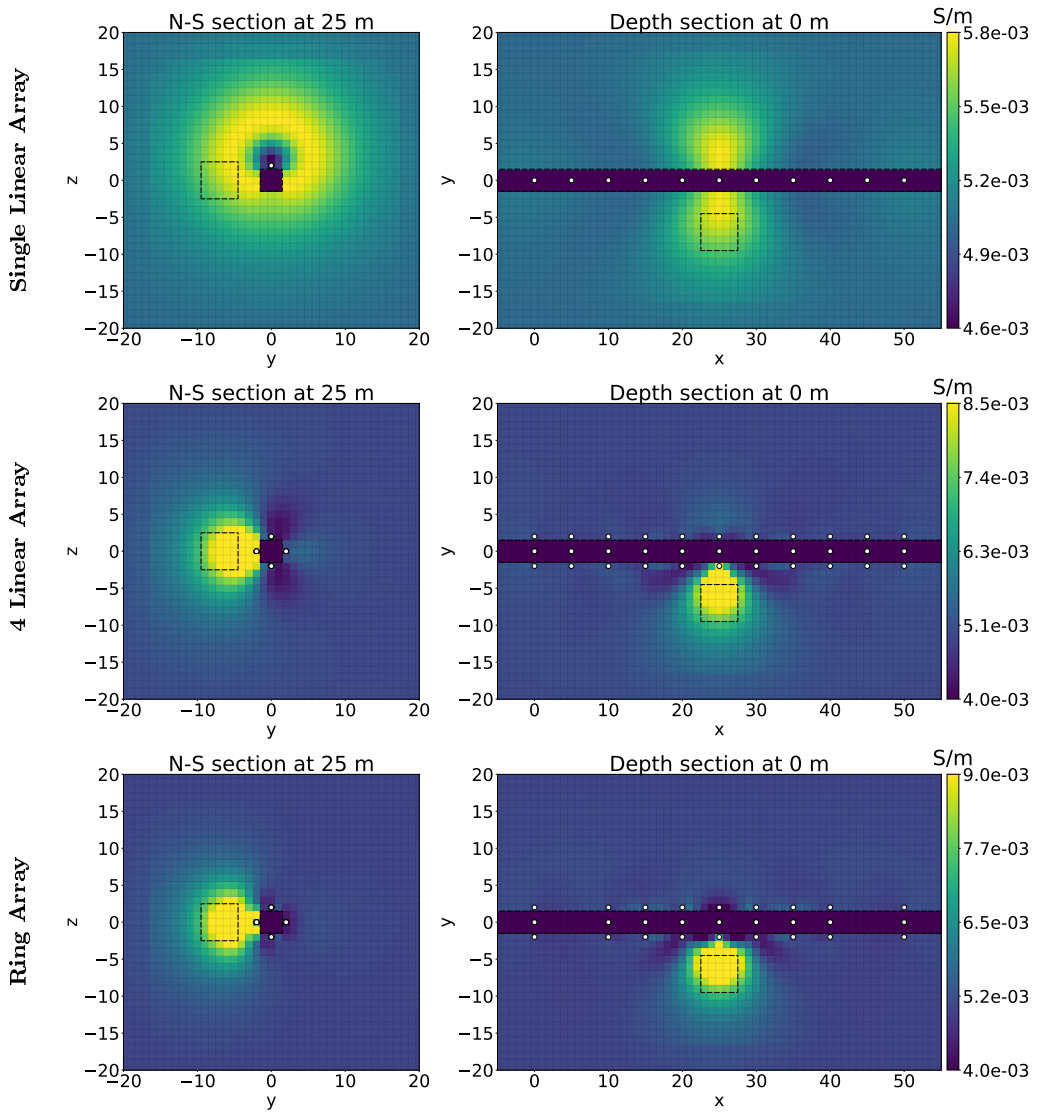


Figure 9:  $x$  and  $z$  sections through the recovered models show how our ability to constrain the location of a conductive block off to the side of the tunnel incrementally improves with the different survey designs. The white dots are projections of the electrode locations onto the section, [the tunnel cells are dark purple](#), and the black dashed outlines show the edges of structures in the true model.

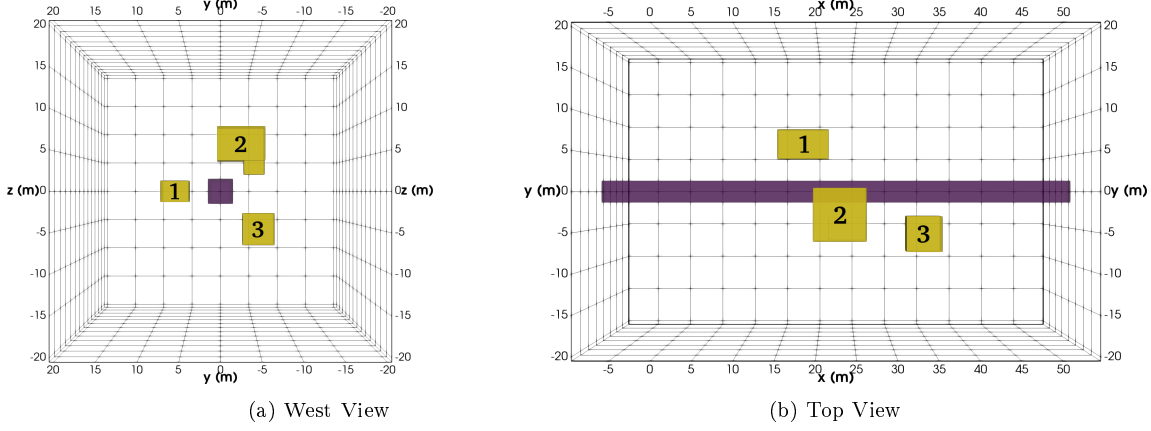


Figure 10: Two orthogonal volumetric cutoff views of the multiple block model. Panel a) shows a view from the west while panel b) shows the model from above. The yellow cells form the 3 blocky conductive structures while the ~~blue~~dark purple cells denote the tunnel. The blocks are labeled 1-3 for ease of identification.

425 ~~cross-sections~~cross sections. The results are therefore presented using thresholded  
 426 volumes that enclose all of the model cells above or below a specified conductivity  
 427 threshold. The dark ~~blue~~purple cells show the resistive air cells, which comprise  
 428 the tunnel, while the yellow and blue-green volumes show regions of high ( $\geq 0.01$   
 429 S/m) and intermediate ( $\geq 0.006$  to  $0.007$  S/m) conductivities, respectively. The first  
 430 column of plots shows a view looking along the tunnel from its western end while the  
 431 second column shows the view from above. The black wire-frames in each plot show  
 432 the true location of the conductive blocks while black dots mark electrode locations.

433 With the single linear array survey, the inversion places a conductive ring around  
 434 the tunnel in the location of block 2 but shows no evidence of blocks 1 or 3. This is  
 435 due to the shielding effect of the tunnel which directs the primary currents ~~upwards~~upward  
 436 and therefore excites comparatively small responses in the blocks located off  
 437 to the side or beneath the tunnel. The 4 linear array survey does a better job of  
 438 identifying the presence of all 3 blocks but the anomalies are smeared together. From  
 439 this result identifying the location of block 3 would be challenging. The inversion  
 440 results of the ring array survey show significant improvements in resolution. We are  
 441 now able to clearly identify each of the blocks as separate and distinct anomalies.  
 442 Although the recovered conductivity of block 3 is smaller than that of the other two  
 443 blocks, there is sufficient resolution to identify it as a separate body.

#### 444 4.1.4. Resolving More Complex “Geological” Structures

445 Having tested the performance of the different surveys on a series of simple syn-  
 446 synthetic models containing conductive blocks, we then designed a more complex model  
 447 with conductive structures meant to mimic water inflow in the potash mine. For this  
 448 synthetic model imagine that water seeped ~~downwards~~downward into the evaporite  
 449 from the overlying aquifer and then found a zone of weakness along a bedding plane  
 450 and flowed diagonally over the top of the tunnel. As the freshwater flowed through the  
 451 salt it dissolved ions into solution and created dissolution cavities until becoming a

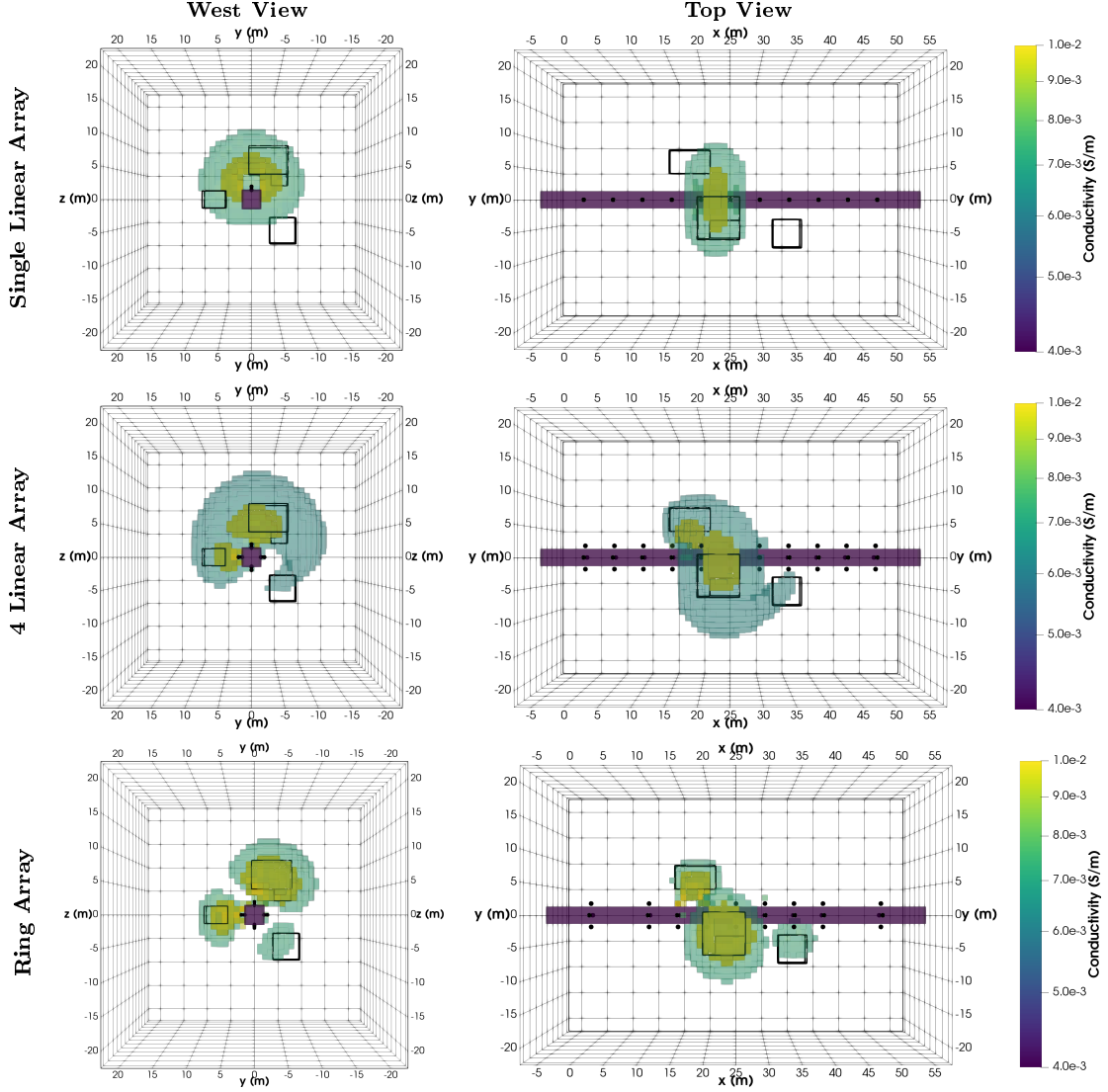


Figure 11: Volumetric cutoff views of the inversion results which show how well each survey recovers the conductive targets within the multiple block model. The left column shows views from the west while the right column shows the model from above. The yellow and blue-green volumes show regions of high ( $\geq 0.01 \text{ S/m}$ ) and intermediate ( $\geq 0.006 \text{ to } 0.007 \text{ S/m}$ ) conductivities, respectively, while the ~~blue~~ dark purple cells denote the tunnel. The black outlines show the true location of the conductive blocks and black dots mark electrode locations.

452 saturated brine. On the south side of the tunnel, the water/brine pooled and seeped  
 453 further into the surrounding salt creating a larger conductive region alongside the  
 454 tunnel. Since the potash mine inspired this model, we will refer to it as the synthetic  
 455 Mosaic model. Figure 12 shows ~~3D~~3-D views of the synthetic Mosaic model with  
 456 the ~~blue~~dark purple cells representing the resistive tunnel cells and the yellow cells  
 457 denoting the wet conductive structure ( $10 \text{ S/m}$ ) in the otherwise resistive dry salt  
 458 background (~~5e~~3.5 $\times 10^{-3} \text{ S/m}$ ).

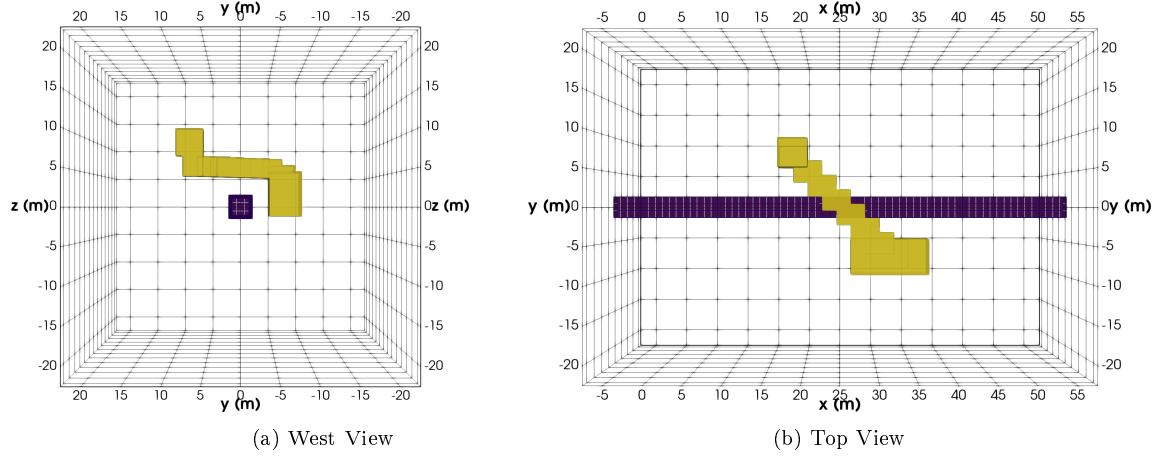


Figure 12: Two orthogonal volumetric cutoff views of the synthetic Mosaic model. Panel a) shows a view from the west while panel b) shows the model from above. The yellow cells form the conductive structure meant to simulate wet regions around the tunnel while the ~~blue~~dark purple cells mark the location of the tunnel.

459 The results of the inversions to test the performance of each survey on this more  
 460 complex model are presented in Figure 13. The ~~3D~~3-D volumetric cutoff views make  
 461 it easier to visualize the geometry of the recovered conductor relative to the tunnel  
 462 and true model outline. Due to the large differences in amplitude among the recovered  
 463 anomalies, different cutoff values were used for high and intermediate conductivities  
 464 in the linear and ring array based models. For the single linear array and the 4 linear  
 465 array results, the high conductivity yellow volumes have conductivities  $\geq 0.02 \text{ S/m}$   
 466 while the yellow volumes in the ring array results have conductivities  $\geq 0.08 \text{ S/m}$ .  
 467 Similarly, the blue-green volumes have conductivities  $\geq 0.01 \text{ S/m}$  in the single linear  
 468 array and the 4 linear array results but conductivities  $\geq 0.022 \text{ S/m}$  in the ring array  
 469 results.

470 The single linear array inversion recovered a conductive ring-shaped anomaly that  
 471 extended symmetrically from the electrodes in the top face of the tunnel (top row  
 472 of Figure 13). This recovered model correctly identifies the general along-tunnel  
 473 location of the conductive target but offers little insight into the target's true shape  
 474 or geometry. As in the previous trials, it is not possible to determine which side  
 475 of the tunnel the conductor is on. The inversion result of the 4 linear array survey  
 476 focuses conductive material to the south and top of the tunnel but does not resolve  
 477 the diagonal trend of the structure running above the tunnel (2nd row of Figure 13).  
 478 With the ring array survey, the location of the recovered anomaly along the south

479 side of the tunnel moves ~~upwards and outwards~~upward and outward away from the  
 480 tunnel to help better constrain the largest portion of the conductive structure (3rd  
 481 row of Figure 13). The recovered anomaly is significantly less smeared out than the 4  
 482 linear array result and begins to convincingly resolve the horizontal conductor which  
 483 passes diagonally over the top of the tunnel.

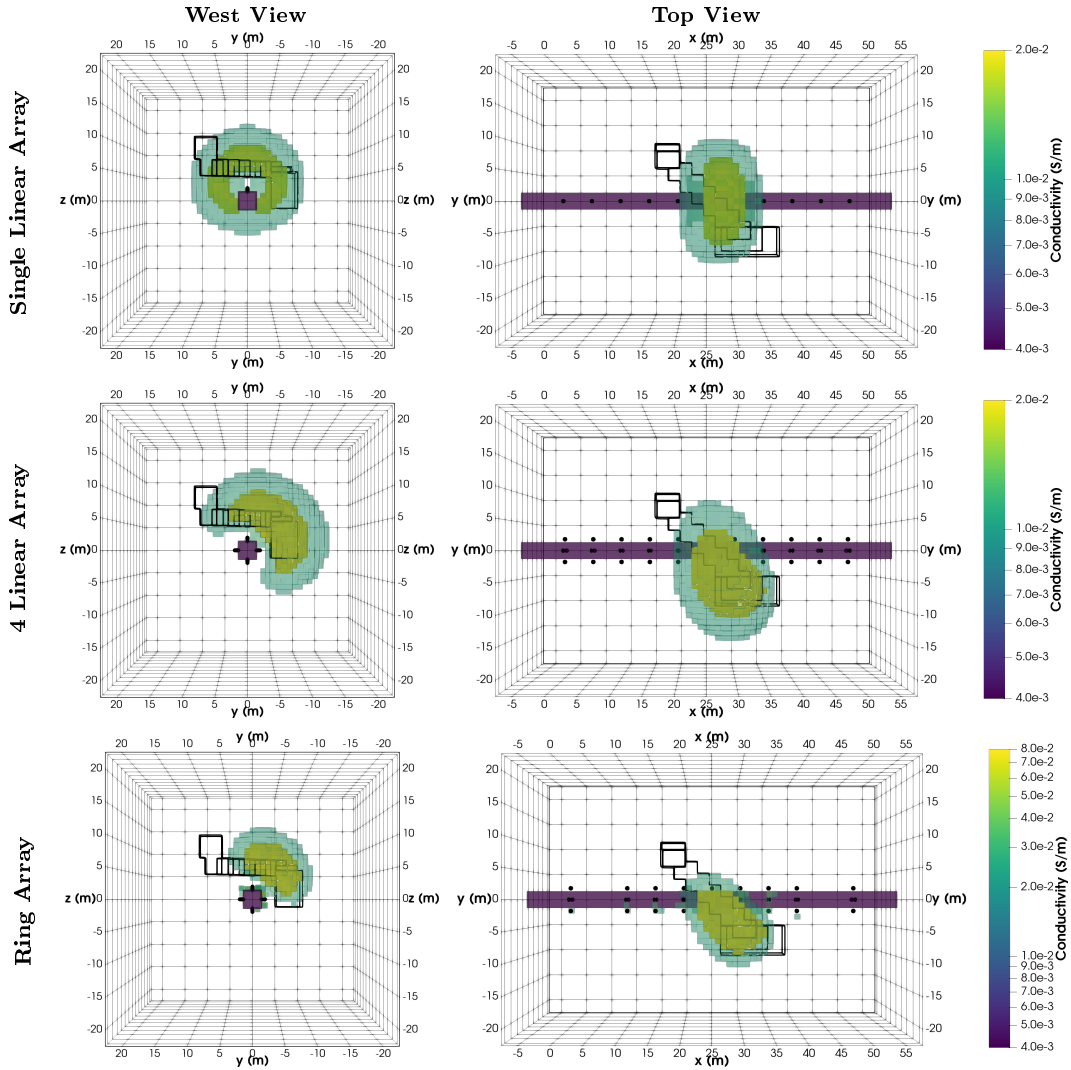


Figure 13: Volumetric cutoffs of the inversion models showing how well each survey recovered the synthetic Mosaic model. The left column shows the models from the west while the right column shows them from above. As in previous tests the yellow and blue-green volumes show regions of high and intermediate conductivity while the ~~blue~~dark purple cells denote the tunnel. The black outlines show the true location of the conductive structure and the black dots mark electrode locations.

#### 484 4.1.5. Summary: Straight Tunnel Synthetics

485 The results of these straight tunnel synthetic tests show that the ring array out-  
 486 performs the single linear array in underground environments. Some of the limitations  
 487 of the single linear array include:

- Inability to constrain the around-tunnel location of anomalies (anomaly smeared around the tunnel to form a conductive ring).
- Anomalies adjacent to faces without electrodes are poorly excited, have much smaller secondary responses, and are poorly resolved in the inversion.
- Inversions greatly underestimate the distance of the anomaly from the tunnel.
- Difficult to differentiate multiple anomalies in the inversion due to smearing.

The ring array helps address all of these limitations and much more accurately resolves the shape and location of anomalies. In situations where anomalous structures are located ~~further-farther~~ away from the tunnel, the use of electrodes in strategically placed off-tunnel boreholes can be used to improve resolution (Mitchell, 2020). Due to the expense and risks sometimes associated with drilling off-tunnel boreholes modeling should be completed first to estimate their situation-specific benefits.

#### 4.2. Horseshoe Tunnel Synthetics

Since many in-mine applications incorporate more complicated tunnel geometries and present the need to image the region between tunnel segments in addition to the region around the tunnel, we created a new synthetic model with a tunnel geometry that resembles an asymmetric horseshoe. This tunnel geometry mimics the more complex tunnel geometry associated with the field dataset from the Mosaic potash mine presented in Mitchell and Oldenburg (2016a,b).

Figure 14 shows an oblique view of the tunnel (~~blue-dark purple~~ volume) and the location of electrodes for each survey (black dots). For the single linear array survey, electrodes were laid out at 5 m intervals along the interior wall of the tunnel. For the 4 ~~Linear~~linear array and ring array surveys electrodes were added to the other faces of the tunnel to form rings of electrodes spaced 5 m apart. As with the straight tunnel tests, all possible 4 electrode dipole-dipole measurements were included for each survey to form a comprehensive dataset. The 4 linear array survey differs from the ring array survey since all of the electrodes utilized in a measurement from the 4 linear array survey must lie in the same face of the tunnel (i.e., all 4 electrodes must reside in the floor, ceiling, or the same sidewall). The ring array, on the other hand, can combine electrodes from multiple faces in a single measurement. As a result, the size of the ring array survey increases substantially as the number of electrodes increases. The size of each survey is summarized in Table 2.

	# <del>Electrodes</del> <ins>Electrodes</ins>	# TX	# TX	# Data	# Data
Single Linear Array	25	300		75,900	
Four Linear Arrays	100	1,200		303,600	
Ring Array	100	4,950		23,527,350	

Table 2: A table showing the size of each survey in terms of the number of electrodes used, the number of TXs, and the total number of data.

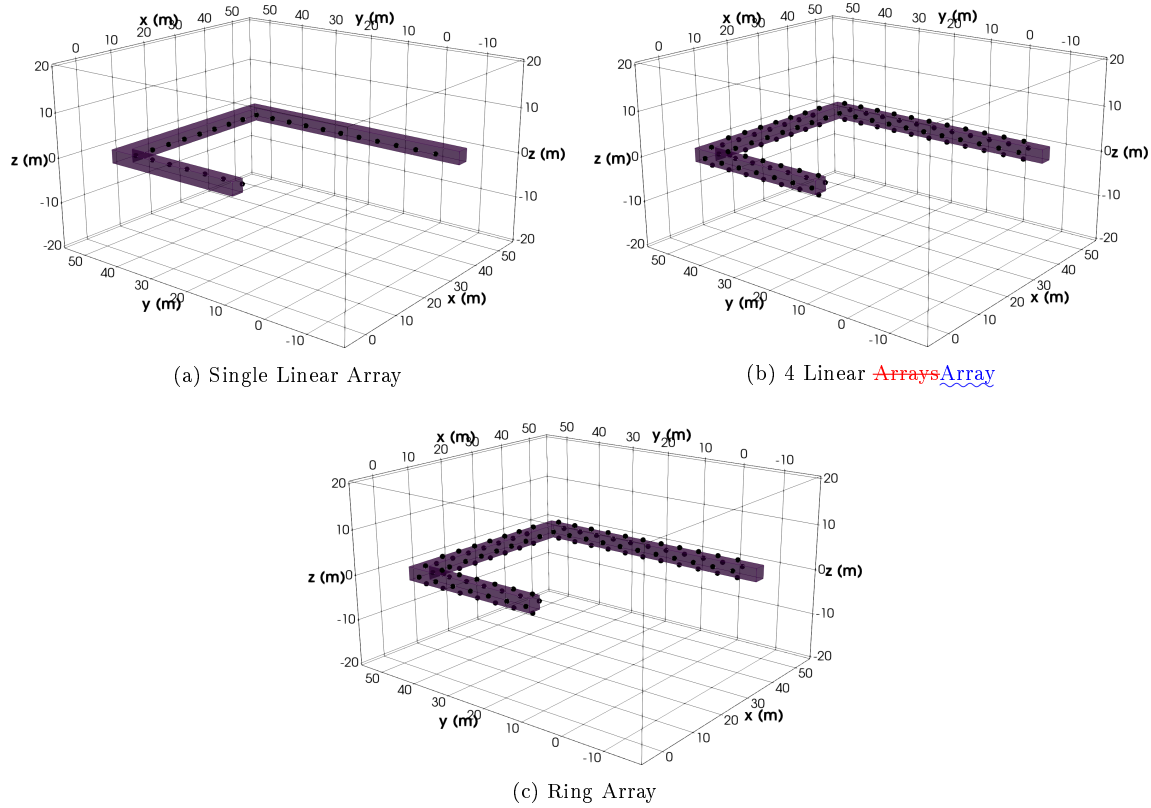


Figure 14: Oblique views of the asymmetric, horseshoe shaped tunnel with electrode locations used by each survey marked using black dots.

520    4.2.1. *Resolving Multiple Bodies or More Complex “Geological” Structures*

521    To test the limitations of these surveys with the more complex tunnel geometry  
522    a synthetic model akin to the synthetic Mosaic model, tested in Section 4.1.4, was  
523    designed. This model contains a conductive structure within the central region be-  
524    tween the tunnels. A large conductive body was placed near the midpoint of the  
525    easternmost branch of the tunnel. From the top of this large conductive body, a 3 m  
526    square conduit extends horizontally to the NW at a height of 4 m above the top of  
527    the tunnel. Once again, this conductive structure was meant to simulate a dissolution  
528    conduit where water from the overlying aquifer flows along a bedding plane in the  
529    salt and then pools or seeps into the surrounding salt to create a larger conductive  
530    region alongside the tunnel. The geometry of this 10 S/m conductive structure within  
531    the ~~5e~~<sup>—</sup>3.5 × 10<sup>-3</sup> S/m background is shown by the black outlines in Figures 15 and  
532    16. As in previous trials, SimPEG was used to forward model synthetic data for  
533    each survey, contaminate it with 2% Gaussian noise, and invert. The results of these  
534    inversions are shown in Figures 15 and 16 where volumetric cutoffs show regions of  
535    high (yellow) and intermediate (blue-green) conductivities. For the high conductivity  
536    yellow volumes cutoff values of 0.015 S/m were used for the single linear array and 4  
537    linear array results while a cutoff value of 0.03 S/m was used for the ring array results.  
538    Cutoff values of 0.01 S/m and 0.015 S/m were used for the intermediate conductivity  
539    blue-green volumes for the linear and ring array results, respectively.

540    With the single linear array, the recovered conductive anomaly is centered about  
541    the plane of the electrodes and extends symmetrically above and below the tunnel.  
542    This limits our ability to differentiate between targets above or below the tunnel.  
543    Although there is some elongation of the anomaly in the NW direction the recovered  
544    model shows very little evidence of the horizontal conduit. The results of the 4  
545    linear array inversion are very similar to the single linear array. The main difference  
546    is a slight shift of the anomaly ~~upwards~~<sup>—</sup>upward which hints at the target’s true  
547    location above the tunnel. With the ring array, the anomaly begins to elongate  
548    to the NW, tracking the location of the horizontal conduit. There is also a clear  
549    shift of the anomaly ~~upwards~~<sup>—</sup>upward which helps us correctly determine that the  
550    conductive structure lies above the tunnel. Although the inversion results greatly  
551    overestimate the thickness of the horizontal conduit there is a notable dip to the  
552    recovered conductor. This shows it sloping ~~downwards~~<sup>—</sup>towards~~downward~~<sup>—</sup>toward the  
553    eastern branch of the tunnel where the large conductive body sits.

554    In this example, the ring array inversion showed marked improvement over either  
555    of the linear array inversions. With the ring array inversion, we can delineate the  
556    NW trend of the horizontal conduit and correctly identify the general location of the  
557    conductive structure above the tunnel.

558    4.2.2. *Summary: Horseshoe Tunnel Synthetics*

559    In these examples with a more complex tunnel geometry, where the region between  
560    tunnels needs to be resolved in addition to the region around the tunnel, the ring  
561    array survey once again outperforms the single linear array survey. In situations  
562    where cross-tunnel measurements are made, the recovered anomalies in the single  
563    linear array inversions remain pinned to the electrode plane regardless of the true  $z$ -

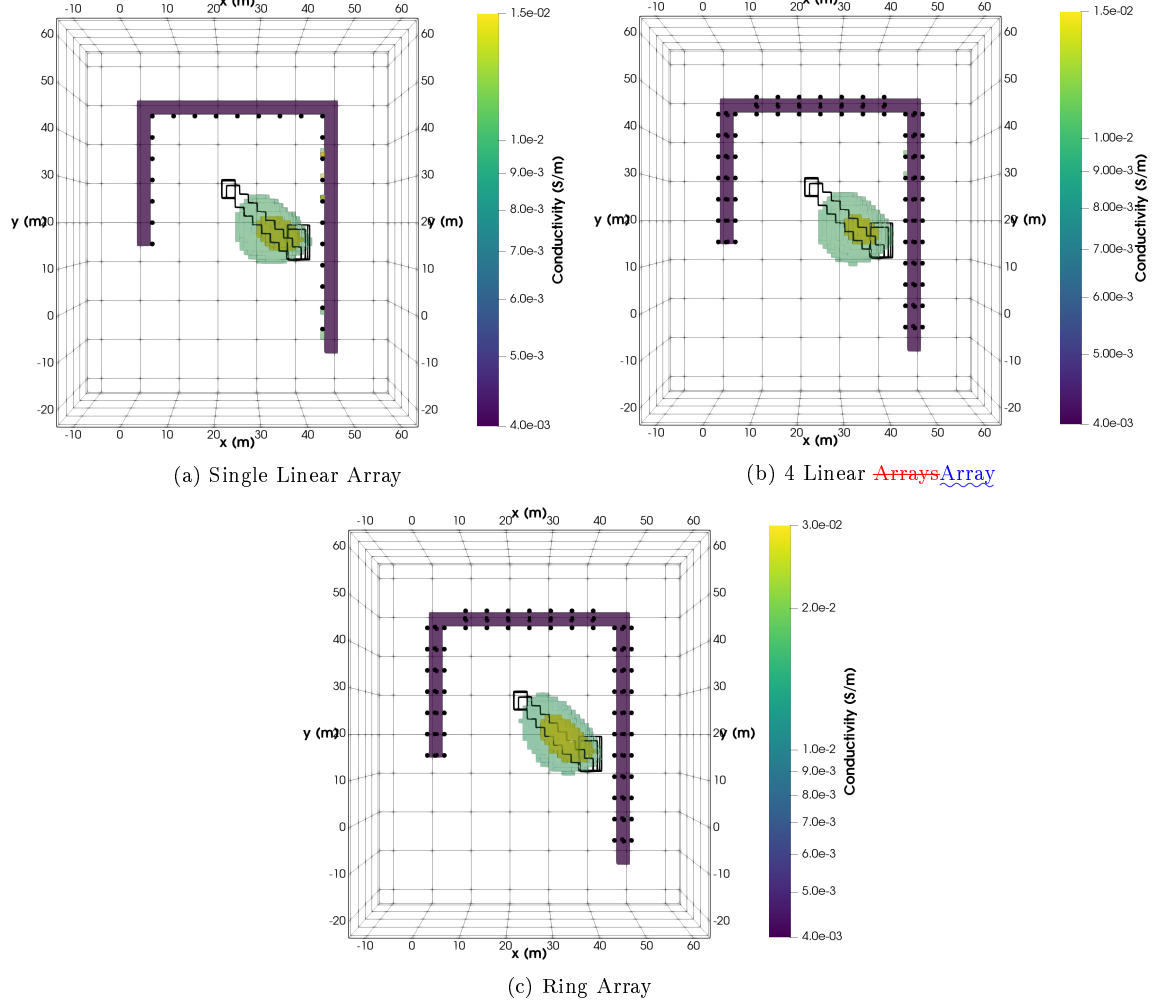


Figure 15: Volumetric cutoffs of the inversion models as seen from above which show how well each survey recovered the synthetic Mosaic model. As in previous tests the yellow and blue-green volumes show regions of high and intermediate conductivities, while the ~~blue~~-dark purple cells denote the horseshoe shaped tunnel. The black outlines show the true location of the conductive structure and the black dots mark electrode locations.

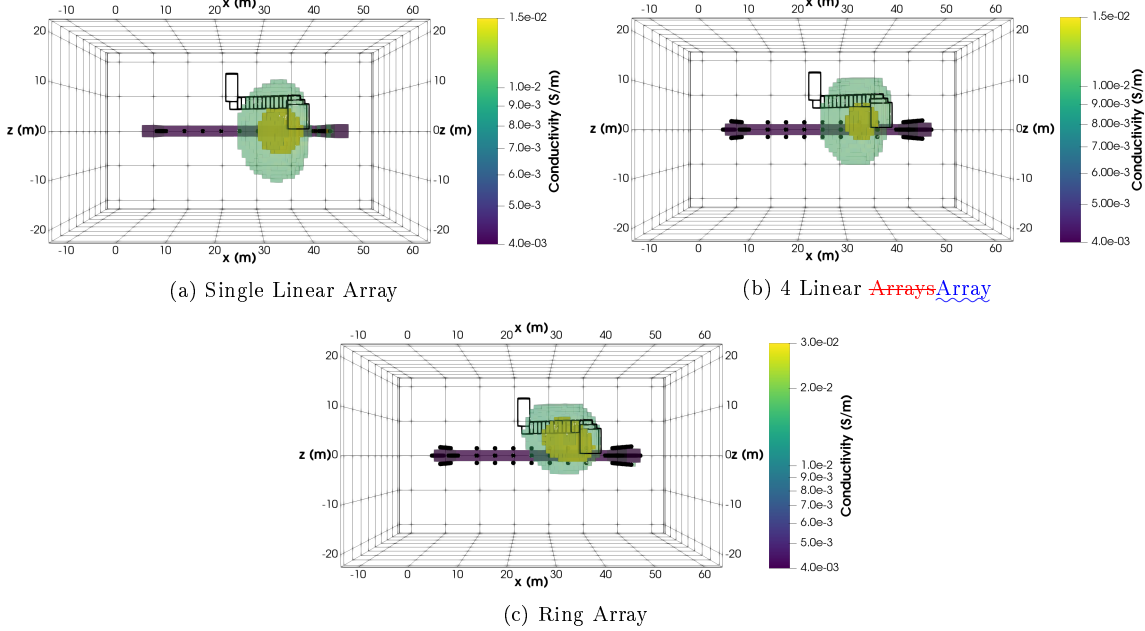


Figure 16: Volumetric cutoffs of the inversion models as seen from the south which show how well each survey recovered the synthetic Mosaic model. As in previous tests the yellow and blue-green volumes show regions of high and intermediate conductivities, while the ~~blue~~dark purple cells denote the horseshoe shaped tunnel. The black outlines show the true location of the conductive structure and the black dots mark electrode locations.

location of the anomaly. The ring array inversion, on the other hand, can differentiate between targets located above and below the electrode plane (see Mitchell (2020) for additional examples and analysis).

#### 4.3. Discussion of Ring Array Testing

In this section, the ring array survey was tested against the single linear array and 4 linear array surveys through the inversion of several synthetic models. For straight tunnels, the main drawback of the single linear array is its inability to constrain the around-tunnel location of anomalous bodies. Although both the 4 linear array and ring array surveys are capable of constraining the around-tunnel location of anomalous bodies, the ring array has higher near-tunnel resolution. This higher near-tunnel resolution is a result of higher sampling densities and a larger, more uniform distribution of sensitivities afforded by diagonal measurements in the ring array. The benefits of this improved near-tunnel resolution are most apparent when trying to resolve complex structures in close proximity to the tunnel such as the multiple block model shown in Section 4.1.3.

For situations in which the target offset from the tunnel is greater than 1.5-2 times the ring spacing, the use of electrodes in off-tunnel boreholes may help to increase sensitivity and improve resolution in these more distant regions of interest. The ring array survey nicely resolves closer proximity targets so the benefits of using off-tunnel boreholes are negligible in these situations. While the placement of electrodes in easily accessible boreholes or tunnel branches can improve our ability to resolve anomalies

585 with larger offsets from the tunnel it is probably wise to delay the drilling of survey  
586 specific boreholes until a reconnaissance survey has been completed. This allows for  
587 a more targeted approach in which off-tunnel boreholes can be used to better resolve  
588 distinct targets.

589 Ring array surveys are also useful for more complex tunnel geometries, such as the  
590 asymmetric horseshoe example in Section 4.2, where cross-tunnel measurements are  
591 made. In these situations, the ring array helps constrain the  $z$ -location of anomalies  
592 between the tunnels allowing anomalies above and below the tunnel to be differenti-  
593 ated. With the single linear array and 4 linear array surveys, the recovered anomaly  
594 remains pinned to the central electrode plane regardless of the conductor's true lo-  
595 cation above or below the tunnel (see Mitchell (2020) for additional examples and  
596 analysis). In these more complex tunnel systems, the ring array will also help resolve  
597 the around-tunnel location of targets which do not lie in the central region between  
598 the tunnels. In this situation, the single linear array will likely recover a smeared ring  
599 of conductive material around the tunnel or fail to recover the anomaly altogether.

600 Having shown that the ring array is better suited for tunnel-based surveys than  
601 the single linear array the next task is to contend with the vastly larger size of the  
602 full/comprehensive ring array survey. To do this we developed a new survey design  
603 methodology. The following section describes how this survey design methodology can  
604 be used to select a subset of TXs and RXs ~~which retain~~ which retains improvements  
605 in model resolution but minimize survey size.

## 606 5. Ring Array Survey Design: Balancing Resolution and Survey Size

607 Although the ring array survey increases near-tunnel resolution and eliminates  
608 non-uniqueness issues associated with the around-tunnel location of targets, the in-  
609 creased size of the ring array survey can be a significant drawback. A comparison  
610 of the size difference between the single linear array and the ring array survey, for  
611 the straight tunnel examples tested in Section 4.1.1, shows that the comprehensive  
612 ring array survey (630 TXs and 353,430 RXs) is about 178 times larger than the  
613 comprehensive single linear array survey (55 TXs and 1,980 RXs). In the context of  
614 time required to collect the survey, this is a significant difference. ~~With the~~ Using the  
615 multi-channel capabilities of the IRIS Syscal Pro Switch system, which allows up to  
616 10 potential differences to be recorded during each current injection, a programmed  
617 sequence of about 30,000 measurements can be collected each day assuming 24-hour  
618 collection with 500 ms injections and 2-6 stacks per measurement. At this rate, the  
619 comprehensive ring array survey would require about 11.8 days to collect, while the  
620 single linear array survey only requires about 1.6 hrs of collection time. Since the  
621 straight tunnel example analyzed here is a fairly small problem with only 36 elec-  
622 trodes a larger ring array survey with 120 electrodes would contain close to 40 million  
623 possible measurements in the comprehensive dataset and be prohibitively expensive  
624 to collect. To make the survey more feasible/economical a subset of the possible  
625 measurements needs to be selected. This selection process is known as survey design.

626 Determining a feasible survey size depends on the size of the area that needs to  
627 be surveyed and the required resolution. For most medium to large sized surveys,

628 collection times of a few days to a week are reasonable.

629 Within the geophysics community, surveys are designed using many different ap-  
630 proaches. Some geophysicists simply create pseudo-random measurement sequences  
631 that utilize all of the electrodes and maintain a variety of electrode separation dis-  
632 tances, while others promote the use of optimal survey design algorithms, as described  
633 by [Curtis \(1999\)](#); [Stummer et al. \(2004\)](#); [Wilkinson et al. \(2006\)](#); [Maurer et al. \(2010\)](#); [Haber et al. \(2012b\)](#), [Wilkinson et al. \(2012\)](#), [Loke et al. \(2014\)](#) and Uhlemann et al.  
634 ([Curtis \(1999\)](#), [Stummer et al. \(2004\)](#), [Wilkinson et al. \(2006\)](#), [Maurer et al. \(2010\)](#),  
635 [Haber et al. \(2012b\)](#), [Wilkinson et al. \(2012\)](#), [Loke et al. \(2014\)](#)) and Uhlemann et al.  
636 (2018). The pseudo-random sequences are fast and computationally inexpensive to  
637 create but can result in larger than necessary surveys that fail to maximize model  
638 resolution. The numerically optimized surveys, on the other hand, do a very good  
639 job of minimizing survey size and maximizing model resolution or data content, but  
640 are often very computationally expensive to create. The computational cost of survey  
641 design becomes especially important when working with large surveys since time and  
642 available memory can limit the size of the problem that it is feasible to work with. To  
643 bridge this gap between approaches, we developed a new physics-based survey design  
644 methodology which focuses on answering the following questions:

- 645 1. How many of the ring array measurements are required to glean most of the  
646 improvements in resolution?
- 647 2. How should we select TXs and RXs which best excite and sample the region of  
648 interest?
- 649 3. How do we strike a balance between improvements in resolution and survey size,  
650 [which may be limited by time and instrumentation](#)?

651 In this survey design methodology, a target test block is moved through the ROI  
652 and its response is forward modeled at each location. TXs [which that](#) best excite  
653 the ROI are selected based upon secondary charge accumulation on the target test  
654 block and RXs are pseudo-randomly selected from a subset of measurements that are  
655 sufficiently sensitive to the test block. This [survey design methodology](#) ensures that  
656 the entire ROI is excited and sampled. To balance resolution and survey size, a series  
657 of surveys with a progressively increasing number of TXs are created and inverted.  
658 The inversion results are compared using the  $L_2$  norm of the difference between each  
659 inversion model and the true model ( $\|\sigma_{inv} - \sigma_{true}\|_2$ ) as a proxy for resolution. The  
660 point at which the addition of more TXs or RXs produces negligible improvements  
661 in resolution is used to determine the preferred survey.

662 Although these subsets may not constitute strictly optimal surveys, this method-  
663 ology is an intuitive, physics-based, computationally inexpensive way to design an  
664 effective survey. With minimal computational cost, we can design small surveys with  
665 comparable resolution to the comprehensive ring array survey. In this physics-based  
666 design methodology, we first focus on selecting TXs that uniformly excite the ROI  
667 and then explore ways to reduce the total number of RXs.

668 5.1. TX Selection

669 When designing a survey we must first ensure that all potential targets within the  
670 ROI are excited by one or more TX. To excite the target, a sufficiently large primary  
671 current density is needed in the vicinity of the target to produce a measurable buildup  
672 of charge on the surface of the anomalous body. If the target is not adequately excited  
673 there will be no secondary fields to measure and therefore no information about the  
674 target.

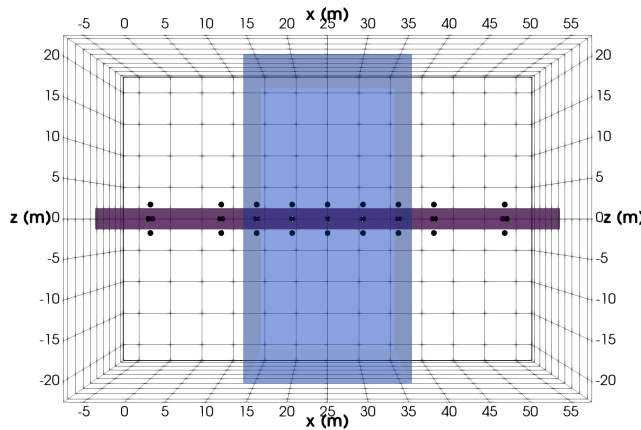


Figure 17: A 3D view of the dark blue-purple tunnel cells, the electrode locations used in the ring array survey (black dots) and a light blue volume showing the defined region of interest (ROI).

675 To select TXs which that have the greatest chance of exciting all potential targets, we must first define the region of interest (ROI). For the straight tunnel examples, the ROI extended from  $x = 15$  m to  $x = 35$  m and from -20 m to 20 m in the  $y$  and  $z$ -directions respectively (see Figure 17). The size and conductivity of a test block to move through the ROI must then be chosen. The conductivity should be chosen to reflect your the best estimate of the target's conductivity. To minimize the number of different test block locations we experimented with 5 and 10 m cubes. Even with this fairly small ROI, this makes a big difference in the number of test blocks that need to be forward modeled. With the 5 m test blocks there could be as many as 256 test blocks in the ROI while with 10 m test blocks there are only 32. Shown in Figure 18 are two potential ways that the ROI could be populated with test blocks. Although there were differences in the selected TXs between the 5 and 10 m test block trials, the performance of the surveys were very comparable. This shows These tests show that the method is not highly sensitive to the chosen test block size and gives the user more freedom to layout a grid of test blocks within the ROI to fit their application. Based on this analysis we recommend a test block size of, test blocks which are roughly 1-2 times the ring separation distance in size yield the best results. In the following trials, the ROI was divided into 10 m test block regions as shown in Figure 18.

694 After determining the test block parameters, we sequentially moved the test block through the ROI to each of its 32 possible locations and forward modeled the response of the test block at each location. We then analyzed the response of each test block

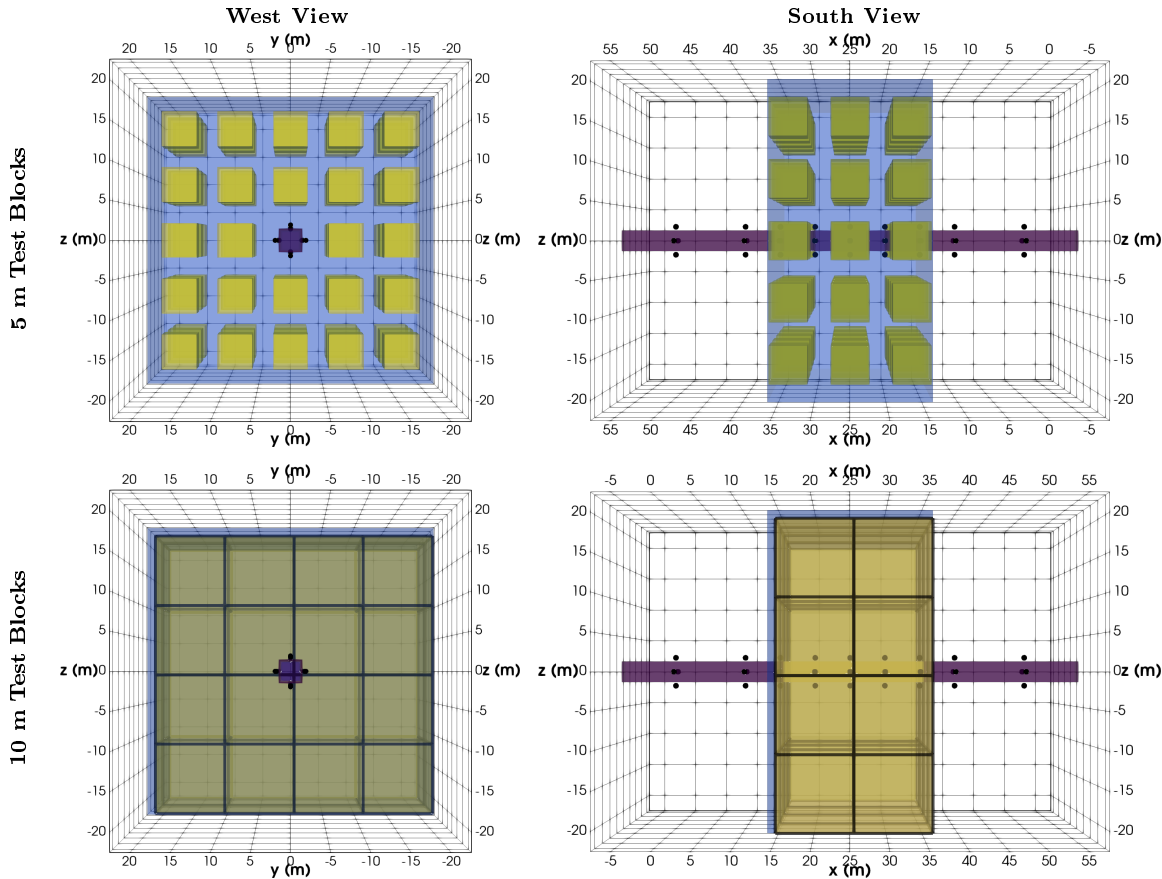


Figure 18: Plots showing 2 different ways that test block locations (yellow cubes) could be allocated within the ROI (light blue volume). In the top row, 5 m cubic test blocks are laid out on a grid with 3 m spaces in between them to fill the ROI with a total of 72 blocks. In the bottom row, 10 m cubic test blocks are placed adjacent to one another with no gaps between them to completely cover the ROI. For reference, the dark blue-purple cells mark the location of the tunnel and the black dots show electrode locations.

697 to a given TX and ranked the TXs based on a series of metrics that quantify how well  
 698 they excite the test block. In total we tested four different metrics: secondary charge  
 699 accumulation, mean secondary current density, cumulative sensitivity, and measured  
 700 data differences.

701 Secondary fields are computed by subtracting the primary field from the total  
 702 field. The secondary charges ( $Q_s$ ) and secondary current density ( $\vec{j}_s$ ) are therefore  
 703 computed using  $Q_s = Q_t - Q_p$  and  $\vec{j}_s = \vec{j}_t - \vec{j}_p$ , respectively. Here, the primary field  
 704 shows the response of the reference model (tunnel in otherwise homogeneous fullspace)  
 705 to the TX, and the total field accounts for the response of the tunnel and the test  
 706 block. The secondary charges and secondary current density, therefore, isolate the  
 707 response of the test block and can be used to quantify how well each TX excites the  
 708 test block at each location within the ROI.

709 The secondary charge ( $Q_s$ ) accumulation for each TX and test block location  
 710 were calculated using the forward modeled values of the secondary electric field ( $\vec{E}_s$ )  
 711 according to the relation,

$$\nabla \cdot \vec{E}_s = \frac{q_s}{\epsilon_0} \quad (5)$$

712 Where where  $q_s$  is the secondary charge density and  $\epsilon_0$  is the electric permittivity  
 713 of free-space. For each cell, the enclosed charge  $Q_s$  was calculated by dividing by  
 714 the cell volume. Since charge is conserved the total sum of positive and negative  
 715 charges over the full model domain should go to 0. However, by only summing the  
 716 positive charges over the surface of the test block we can determine which transmitter  
 717 excites the largest secondary response from each test block. Similarly, the secondary  
 718 current density ( $\vec{j}_s$ ) is computed using the constitutive relation  $\vec{j}_s = \sigma \vec{E}_s$ . Computing  
 719 the mean  $\vec{j}_s$  over the interior of the test block provides a measure of the secondary  
 720 current strength that each TX produces within a given test block. Large secondary  
 721 charge accumulations and mean secondary currents indicate that the associated TX  
 722 strongly excites the test block.

723 To compute the cumulative sensitivity we calculated the integrated sensitivity ( $S$ ),  
 724 which measures the cumulative data response to a model perturbation (Kaputerko  
 725 et al., 2007), for each TX assuming a fullspace plus tunnel conductivity model. The  
 726 integrated sensitivity ( $S$ ) ~~can~~ be calculated using the following equation.

$$S = \sqrt{\sum_i J_{ij}^T J_{ij}} \quad (6)$$

727 This equation sums the sensitivity of all the data for each model cell and returns  
 728 a vector which is the number of model cells in length and can be plotted in the same  
 729 manner as the conductivity model. For each test block location, we then summed  $S$   
 730 over the cells within the test block to estimate the cumulative sensitivity of each TX  
 731 to that test block. The logical argument is that the TX with the highest cumulative  
 732 sensitivity is the TX, whose secondary response from the test block created the largest  
 733 change in potential differences at the RXs.

734        The final metric we tested focused on measured data differences. Using the forward  
 735 modeled potential differences from the test block at each of its designated locations,  
 736 we determined the number of “detectable” data associated with each TX.~~To~~,to be  
 737 characterized as detectable  $|\phi_t - \phi_p| = |\phi_s| \geq 1$  mV and  $|\phi_s|/|\phi_p| \geq 0.1$ . For each test  
 738 block, the TX with the largest number of detectable data was deemed to be the best  
 739 TX for exciting that block.

740        Surveys were then incrementally built up, for each of the selection metrics, by  
 741 adding the best TXs for each test block to a list of potential TXs. Once more the half  
 742 of the TXs from a symmetric set of TXs with the same AB separation are flagged, the  
 743 complete set of TXs are added to the subset of selected TXs. TXs are added in this  
 744 manner to uniformly excite the region around the tunnel and create a more uniform  
 745 distribution of sensitivities. This helps avoid the type of artifacts and non-uniqueness  
 746 issues shown in Section 3.1.

AB Separation m	AB Separation [m]	Ratio of Selected TX	Ratio of Selected TX	Rings Used	Rings Used
	2.83		4/8		4 & 6
	5.74		4/16		4-5 & 6-7
	30		8/8		1-6 & 4-9
	30.13		3/16		1-6 & 4-9
	35.11		5/16		1-7 & 3-9

Table 3: A summary of the 24 unique TXs that were identified by taking the single best TX for each test block based on the secondary charge accumulation metric. The first column specifies the AB separation of the TXs, the second column specifies the ratio of selected TXs to the number of TXs in the symmetric subset, and the third column defines the electrode rings which are included in the symmetric subset of TXs.

747        Using the charge metric as an example, we start by looking at the single best TX  
 748 for each test block location. This results in a list of 24 unique TXs with 5 different  
 749 AB separations. These TXs are shown in Figure 19 and described in Table 3. At  
 750 this stage, only the symmetric subset of TXs with an AB separation of 30 m that  
 751 use rings 1-6 and 4-9 was added to the charge based TX subset. None of the other  
 752 subsets had more than half of their TXs selected.

753        We then expand the list of selected TXs by taking the 2 best TXs for each test  
 754 block location. With the new list of prospective TXs, any symmetric sets of TXs,  
 755 with more than 50% of their TXs selected, were added to the survey. The process  
 756 continued by taking the 3 best TXs for each test block location and so on until we  
 757 had a total of 150-160 symmetrically distributed TXs in the charge based subset. To  
 758 characterize how the resolution of the ring array survey changed as a function of the  
 759 number of TXs utilized, five surveys were created from this subset of TXs. As shown  
 760 in Table 4 survey 1 contained the top 30-40 TXs, survey 2 contained the TXs from  
 761 survey 1 plus the next best 30-40 TXs, and so forth up to survey 5 which contained  
 762 the best 150-160 TXs.

763        Figure 20 shows the symmetric sets of TXs that made up the Charge 1 survey.  
 764 In conjunction with this, Table 5 details the order in which symmetric sets of TXs  
 765 were added to the charge based subset and shows how these TXs were split into five

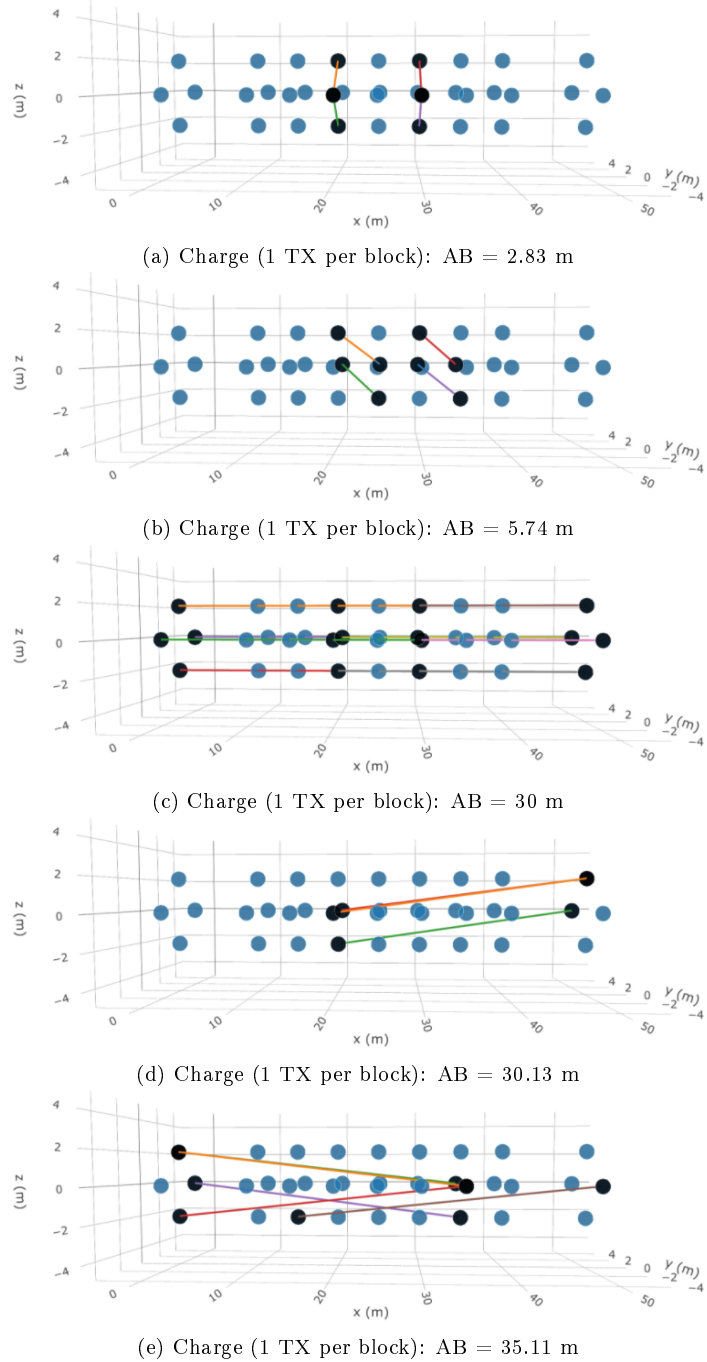


Figure 19: A series of plots showing the 24 unique TXs identified by taking the single best TX for each test block as identified by the secondary charge accumulation metric. Each plot shows the selected TXs with a different AB electrode separation distance. Here the black spheres show electrode locations, which are used as A or B electrodes by the selected TXs, the colored lines represent the TXs and connect their associated A and B electrodes. The blue spheres show electrode locations which are not used by the selected TXs.

<u>Survey ID</u>	<u>Survey ID</u>	# TX	# TX
1		30-40	
2		60-70	
3		90-100	
4		120-130	
5		150-160	

Table 4: This table specifies the number of transmitters in each of the tested surveys. Since TXs are added to the list of selected TXs in symmetric sets based on their AB separations the size of the surveys as shown in Table 5 sometimes falls slightly outside of these target ranges.

766 surveys.

<u>Survey ID</u>	<u>Survey ID</u>	# TXs per Block	# TXs per Block	AB Offset [m]	AB Offset [m]	Rings Used	Rings Used	# TXs in S
1		1		30		1-6 & 4-9		
1		2		5.74		4-5 & 6-7		
1		2		30.13		1-6 & 4-9		
2		3		2.83		4 & 6		
2		3		35		1-7		
2		3		35.11		1-7 & 3-9		
3		4		5		4-5 & 6-7		
3		4		30.26		1-6 & 4-9		
3		4		35		1-9		
3		5		5.74		3-4 & 5-6		
4		6		2.83		5 & 7		
4		6		20		4-8		
4		7		20.2		4-8 & 6-9		
5		8		5		3-4 & 5-6		
5		8		20		1-4 & 2-6 & 6-9		
5		8		25		1-5 & 2-7		

Table 5: This table shows how symmetric TX sets were gradually added to the charge based subset of selected TXs and details which TXs are included in each of the 5 surveys. The colors group TXs, which were added to make each survey.

767 This same process was completed for each of the TX selection metrics discussed  
 768 above and 5 surveys of comparable size were created for each metric. To compare the  
 769 resolving power of each survey SimPEG was used to forward model synthetic data for  
 770 the multiple block model, add 2% Gaussian noise, and invert the synthetic data. This  
 771 is the same multiple block model that was described in Section 4.1.3. It contains three  
 772 conductive blocks of different shapes and sizes that were placed at different locations  
 773 around the tunnel. Block 1 sits along the north side of the tunnel, block 2 is located  
 774 above the southern edge of the tunnel, and block 3 was placed below and to the south  
 775 of the tunnel.

776 To quantify the differences between inversion results from different surveys, we  
 777 found it useful to look at the  $L_2$  norm of the difference between the inversion model  
 778 and the true multiple block model. Although we also experimented with several different  
 779 metrics including the infinity norm of the model differences,  
 780 cross-correlations of the models, and cross gradients of the model the results of all  
 781 these methods of analysis models, all of the results were fairly similar. Figure 21 shows  
 782 the  $L_2$  norm of the differences between each inversion model and the true multiple

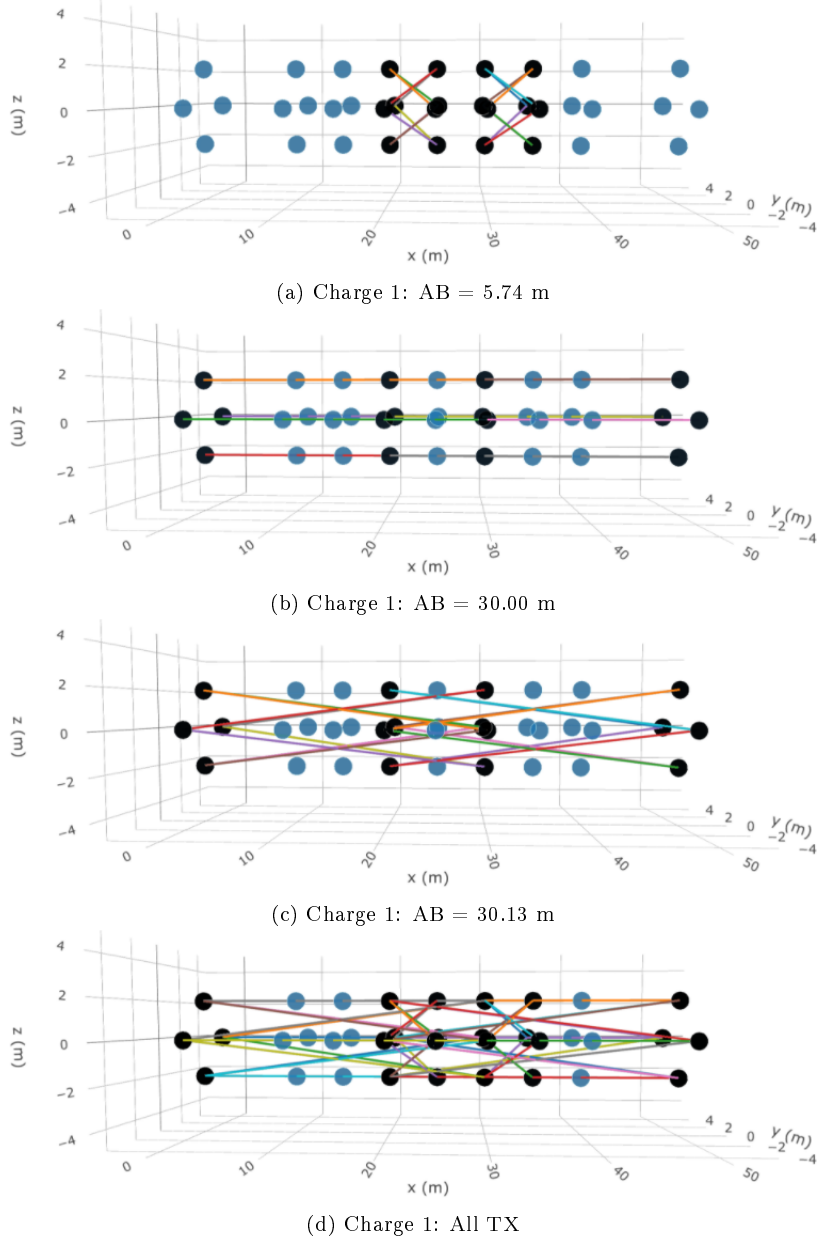


Figure 20: A series of plots showing the symmetric sets of TXs which make up the Charge 1 survey. These are the 40 best TX for uniformly exciting the ROI as determined by the secondary charge accumulation metric. As in Figure 19 the black spheres show A or B electrode locations for the selected TXs, the colored lines represent the TXs and connect their associated A and B electrodes. The blue spheres show unused electrode locations.

783 block model ( $\|\sigma_{inv} - \sigma_{true}\|_2$ ). Before taking the norm of the differences, ~~each of~~  
 784 ~~the models was normalized so that the models were normalized so~~ their values ranged  
 785 between 0 and 1. Normalization scaled the models to ensure that the magnitude of the  
 786 variations within each model was comparable. In this plot, the resolution of the model  
 787 increases as the norm of the model difference decreases since with perfect resolution  
 788  $\sigma_{inv} = \sigma_{true}$  and the difference would be 0. The black, blue, and green dashed lines  
 789 provide proxies for the resolution of the single linear array, 4 linear ~~arraysarray~~, and  
 790 full ring array surveys, respectively.

791 As qualitatively shown in Figure 11, a clear increase in resolution from the sin-  
 792 gle linear array to the 4 linear array survey and from the 4 linear array survey to  
 793 the full ring array survey is observed. The flattening of the solid blue (cumulative  
 794 sensitivity), green (data differences), black (secondary charge), and magenta (mean  
 795  $\vec{j}_s$ ) curves after survey 2 shows that for surveys larger than survey 1 or ~~survey~~-2 the  
 796 norm of the difference between the models decreases very little as additional TXs are  
 797 incorporated. Although there are slight differences between these curves, the resolu-  
 798 tion of the recovered models approached the resolution of the full ring array survey  
 799 for all of the TX selection metrics tested after survey 2. This suggests that with only  
 800 30-70 of the 630 TXs in the full ring array we can glean most of the improvements in  
 801 resolution offered by the full ring array survey.

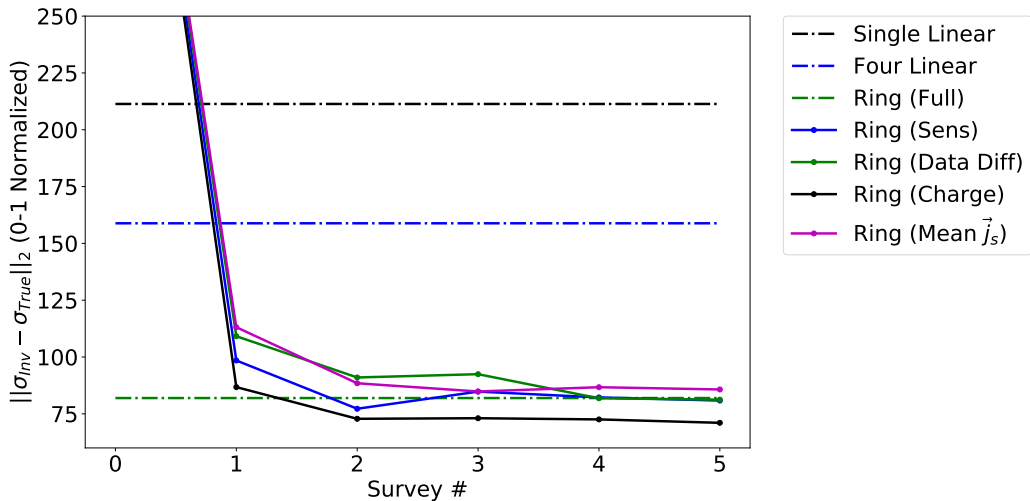


Figure 21: A plot showing the  $L_2$  norm of model differences between the recovered model and the true model. The models have been normalized so that all values of the true and recovered model fall between 0 and 1. This plot shows how well the recovered models from each of the tested surveys recovered the conductive blocks in the synthetic model and allow us to numerically compare these results with those of the single linear array, 4 linear ~~arraysarray~~, and full ring array surveys.

802 Figure 22 shows the minute differences between the full ring array inversion model  
 803 and the recovered models from the Charge 1, 2, and 3 surveys. Other than a small  
 804 increase in the recovered conductivity of blocks 1 and 3, which is observed as the  
 805 number of TXs increased, the models are nearly identical. This visual comparison  
 806 of the recovered models supports the quantitative estimates of model resolution in  
 807 Figure 21 and shows that, for the multiple block model, the addition of TXs to the

TX Selection Methodology
<ol style="list-style-type: none"> <li>1. Choose test block parameters (block size, conductivity, and a grid of locations within ROI).</li> <li>2. Move the test block through the ROI and forward model responses (fields and comprehensive dataset).</li> <li>3. For each TX compute the amount of accumulated secondary charge on the given test block and rank TXs accordingly.</li> <li>4. Incrementally build up a list of the best TXs for each block, starting with the single best TX, then the best 2 TXs, and so forth. Add symmetric sets of selected TXs to create a series of surveys with progressively more TXs.</li> <li>5. For each survey forward model data using the synthetic model, add noise, and invert the data.</li> <li>6. Compare the inversion results of each survey using <math>\ \sigma_{inv} - \sigma_{true}\ _2</math> plots and visual differences to determine the point of diminishing returns (i.e., where the addition of more TXs has a minimal impact on resolution).</li> </ol>

Table 6: Workflow summarizing the steps in the TX selection methodology.

808 Charge 1 survey provides little benefit. In terms of reducing Such a large reduction  
 809 in the size of the ring array survey, this is very significant. It indicates that for this  
 810 particular application, only 40 of the 630 TXs in the full ring array are needed. This  
 811 which equates to just over 6% of the TXs.

812 A visual comparison of the inversion results from each of the different TX selection  
 813 metrics shows only small differences among the recovered models (see Mitchell (2020)).  
 814 Although the shape and location of the recovered conductive anomalies are nearly  
 815 identical across all of the recovered models, small differences in the amplitude of the  
 816 recovered conductivities for blocks 1 and 3 are observed. If we visually rank these  
 817 models, the Charge 1 model appears to have the best resolution, followed by the  
 818 Sensitivity 1, Data Difference 1, and Mean  $\vec{j}_s$  1 models. Although this visual ranking  
 819 is subjective, it is supported by the quantitative measures shown in Figure 21. The  
 820 correlation between the  $\|\sigma_{inv} - \sigma_{true}\|_2$  values and small differences observed in the  
 821 recovered models lends credence to the use of this metric as reliable proxy for model  
 822 resolution.

823 Since the accumulated secondary charge metric performed better than the other  
 824 metrics tested and is less expensive to compute than the cumulative sensitivity, it is  
 825 our method of choice for selecting a subset of TXs which uniformly excite the region  
 826 of interest. The full TX selection methodology, which we described and tested in this  
 827 section, is summarized in Table 6.

828 Having effectively chosen a subset of TXs which reduced the overall size of the ring  
 829 array survey by almost 94% but retained most of the full ring array's resolution we  
 830 have clearly, we have shown that many of the TXs were redundant. In the next  
 831 section, we set out to determine if the size of the ring array survey can be further  
 832 reduced by decreasing the number of RXs associated with each TX.

### 833 5.2. RX Selection for each TX

834 Although the TX selection process greatly reduced the size of the ring array survey,  
 835 there are still 22,440 RXs associated with the Charge 1 survey since a comprehensive  
 836 set of 561 dipole RXs were collected for each TX (see Table 7). Since this straight

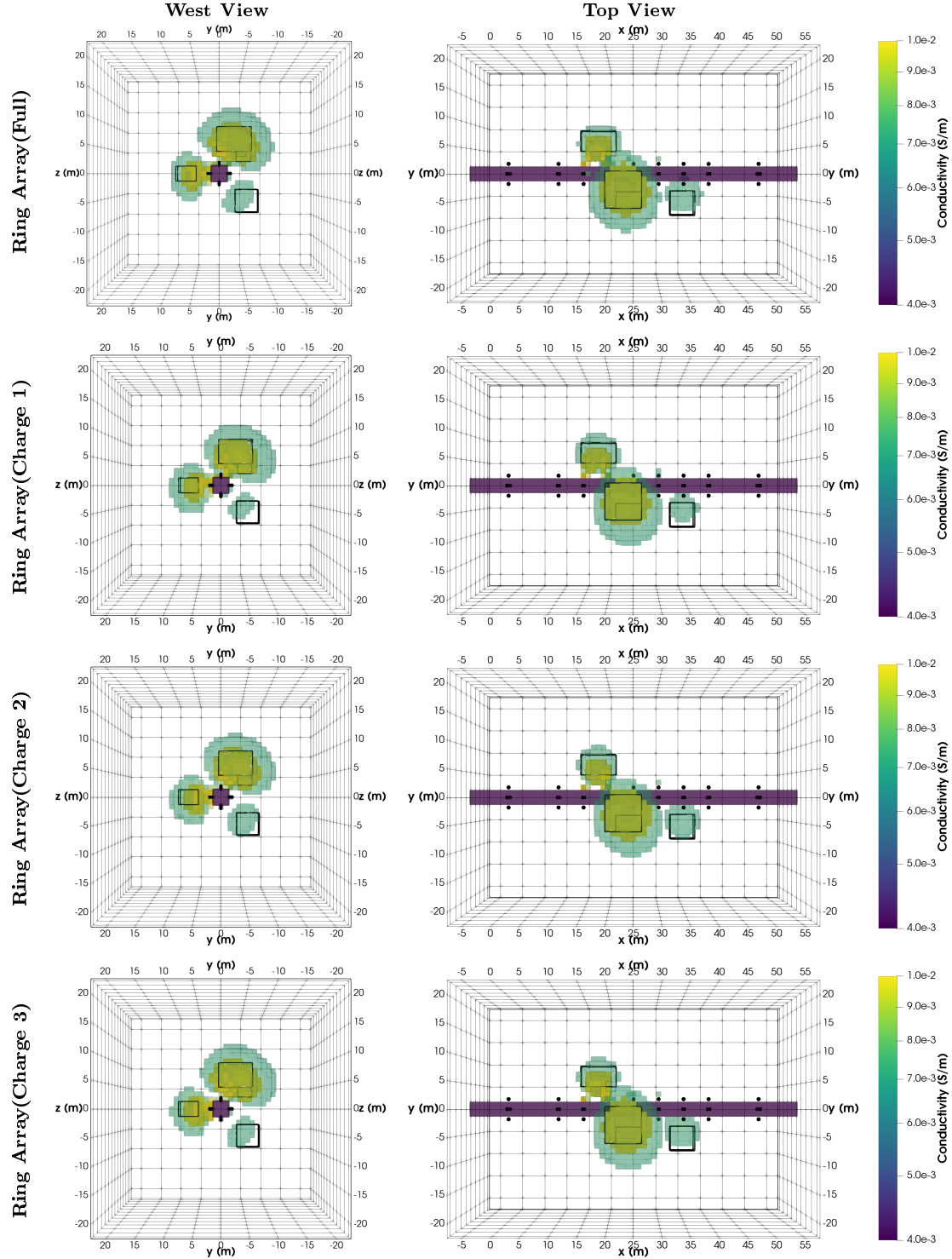


Figure 22: Volumetric cutoff views of the inversion models from the full ring array survey and the Charge 1, 2, and 3 surveys. Regions of high conductivity ( $\sigma \geq 0.01 \text{ S/m}$ ) are shown in yellow and regions of intermediate conductivity ( $\sigma \geq 0.007 \text{ S/m}$ ) in blue-green. The small differences in the recovered models indicate that the resolution of these surveys is comparable. Blue cells denote the tunnel, the black outlines show the true location of the conductive structures, and the black dots mark electrode locations.

tunnel example is still a reasonably small problem, with only 36 electrodes, the need to also reduce the number of RXs becomes more important as the number of electrodes increases.

Here we test one way of pseudo-randomly selecting RXs based on the forward modeled data from the test blocks in the TX selection process against a purely random selection method. In both cases, the survey is built up by adding a set number of RXs for each selected TX. Surveys with 10, 20, 30, 40, 50, 75, 100, 150 and 250 RXs per TX were created to determine how the resolution of the model changes as a function of the number of RXs. This incrementally increasing the number of RXs provides an estimate of how many of the 561 possible RXs per TX can be removed without substantially reducing model resolution. The purely random selection method will be used as a control, against which we can gauge the benefits of the data-based RX selection process.

In the data-based methodology, we first need to form a subset of detectable RXs. For each TX a subset of possible RXs is formed by identifying those RXs which had a detectable response to one or more of the 32 test blocks used in the TX selection process. As for the data difference metric in the TX selection process, a measurement is deemed detectable if  $|\phi_t - \phi_p| = |\phi_s| \geq 1 \text{ mV}$  and  $|\phi_s|/|\phi_p| \geq 0.1$ . To test the sensitivity of this RX selection process to the test block size and the  $|\phi_s|/|\phi_p|$  tolerance, trials were run using 5 and 10 m test blocks along with  $|\phi_s|/|\phi_p|$  tolerances of 5 and 10%. The observed differences were negligible indicating that this method is not highly sensitive to our choice of these parameters. When selecting detectable RXs it is probably best to preclude highly noise susceptible measurements, such as those with high geometric factors.

The detectable RXs are then binned based on their MN offsets (i.e., the distance between the two potential electrodes) and an equal number of RXs are randomly selected from each bin. The number of RXs selected per bin is determined by dividing the number of RXs per TX by the number of MN offset bins. If the number of RXs per bin is greater than the number of possible RXs in a particular bin then random RXs are selected from other bins to ensure that each TX ends up with the specified number of RXs per TX. It is important to maintain an equal number of RXs for each TX to evenly sample the ROI. Since each TX was selected based on the way it excited a different test block giving one TX fewer RXs than other TXs could decrease the sensitivity of the survey to a target in one or more of the test block locations. The hope is that this RX selection process provides a subset of RXs for each TX, which are sensitive to all of the test block locations within the ROI and evenly cover the full range of MN separation distances.

To test the performance of this RX selection process against a purely random approach surveys with 10, 20, 30, 40, 50, 75, 100, 150 and 250 RXs per TX were created. As in the TX selection process, SimPEG was used to forward model synthetic data from the multiple block model, add 2% Gaussian noise, and invert the data. Since there is an element of randomness in each of these RX selection methods this process was repeated 50 times for each method and each size of survey to get a statistical estimate of the variation among the results.

The results of all of these inversions are shown in Figure 23 using the  $L_2$  norm

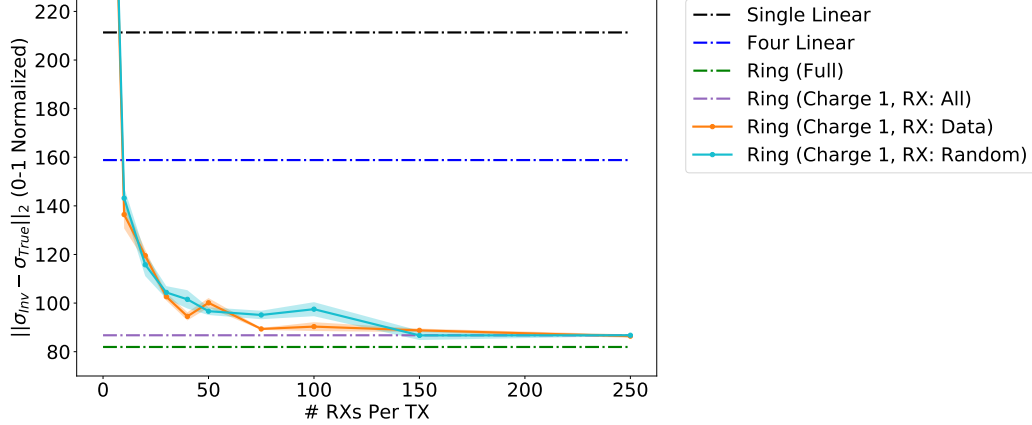


Figure 23: A plot which shows showing the  $\|\sigma_{inv} - \sigma_{true}\|_2$  for inversions of data from surveys with a progressively larger number of RXs per TX. Prior to taking the norm of the difference, all of the models were normalized so that their values varied between 0 and 1. These curves show that for both the data-based (orange) and the purely random (cyan) RX selection processes there are diminishing improvements in resolution for more than 40-50 RXs per TX for these tests with the multiple block model.

of the differences between each inversion model and the true multiple block model,  $\|\sigma_{inv} - \sigma_{true}\|_2$ . To account for variations in scale the models were normalized so that all values ranged between 0 and 1 before computing the norm of the differences. The orange curve shows the performance of the data-based approach and the cyan curve shows the performance of the purely random RX selection process. The shaded regions around each of these curves provide a measure of the variation among the inversion results by showing one standard deviation above and below the mean norm of the model differences. The black, blue, green, and magenta dashed lines provide comparisons of the relative resolution of the single linear array, 4 linear arrays, full ring array, and ring array (Charge 1) surveys, respectively. After 40-50 RXs per TX, the orange and cyan curves flatten and approach the resolution of the Charge 1 survey. This indicates The flattening of the curves indicate that the addition of more RX-RXs does little to improve the resolution of the recovered model.

Figure 24 shows the differences between the mean recovered models from the data-based 10, 40, and 150 RX-RXs per TX trials. A visual analysis of these results supports the  $\|\sigma_{inv} - \sigma_{true}\|_2$  values. An increase in model resolution is observed from 10 to 40 RXs per TX but little improvement is seen between 40 and 150 RXs per TX. Analogous to the TX selection process, as the size of the survey increased the shape and location of the recovered anomalies remain similar but the amplitude of the recovered conductivities for blocks 1 and 3 increased slightly. These changes are most notable for block #3, which is located near the eastern edge of the ROI. This block is not recovered by the 10 RXs per TX survey but is similarly resolved by the 40 and 150 RXs per TX surveys. The success of these RX selection trials once again allows us to significantly reduce the size of the survey, as shown in Table 7. With only 40 TXs and 1,600 data the Charge 1, 40 RXs per TX survey is smaller than the comprehensive single linear array survey but still maintains comparable resolution to

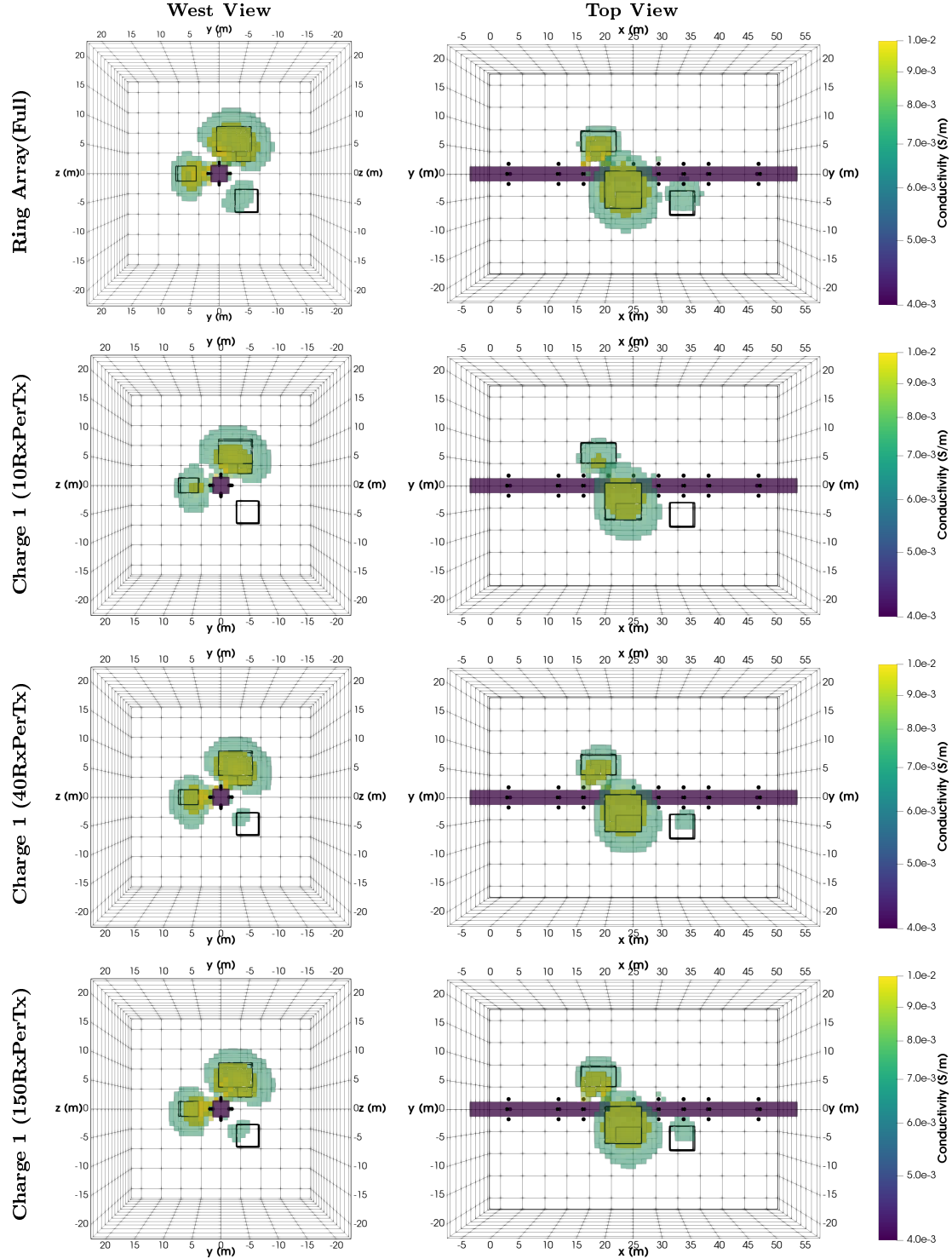


Figure 24: Volumetric cutoff views of the inversion models from the full ring array and data-based RX selection surveys with 10, 40, and 150 RXs per TX from the Charge 1 survey, respectively. Block #3 is resolved using 40 and 150 RXs per TX but not with 10 RXs per TX. Regions of high conductivity ( $\sigma \geq 0.01 \text{ S/m}$ ) are shown in yellow and regions of intermediate conductivity ( $\sigma \geq 0.007 \text{ S/m}$ ) in blue-green. Blue cells denote the tunnel, the black outlines show the true location of the conductive structures, and the black dots mark electrode locations.

908 the full ring array survey.

	# Electrodes	# TX	# Data
Single Linear Array	11	55	1,980
Ring Array (Full)	36	630	353,430
Ring Array (Charge 1)	36	40	22,440
Ring Array (Charge 1, 10 RX Per TX)	36	40	400
Ring Array (Charge 1, 40 RX Per TX)	36	40	1,600
Ring Array (Charge 1, 150 RX Per TX)	36	40	6,000

Table 7: A table showing the size of each of the surveys tested in terms of the number of electrodes used, the number of TXs, and the total number of recorded data.

909 Having shown that these RX selection methods can be used to significantly re-  
 910 duce the size of the survey while still retaining most of the resolution of the full  
 911 ring array model, we now need to compare the performance of the pseudo-random,  
 912 data-based method and the purely random Rx-RX selection method. The orange and  
 913 cyan curves in Figure 23 show that the data-based method (orange curve) generally  
 914 produced models with slightly lower mean  $\|\sigma_{inv} - \sigma_{true}\|_2$  values and had less varia-  
 915 tion among the 50 pseudo-randomly generated surveys. To determine if these small  
 916 differences in the mean  $\|\sigma_{inv} - \sigma_{true}\|_2$  values constitute a meaningful difference in  
 917 model resolution, we visually compared the inversion models from the data-based and  
 918 purely random surveys with 40 RXs per TX in Figure 25.

919 Although the observed differences in these models are small, the data-based Rx-  
 920 RX selection survey is better able to resolve block #3, which was the hardest of the  
 921 three blocks for all of the surveys to constrain due to its location near the edge of  
 922 the ROI. In addition to slightly better resolution, there is also less variation among  
 923 the recovered models from the pseudo-random data-based RX selection method. Due  
 924 to these advantages and the negligible difference in computational cost between the  
 925 two methods we recommend the pseudo-random, data-based method is preferred over  
 926 the purely random RX selection method. The differences in computational costs are  
 927 negligible since the forward modeling of each test block was already completed during  
 928 the TX selection process.

929 The results in this section clearly show that a comprehensive set of dipole RXs is  
 930 not always required for each TX. For the multiple block model tested here, most of  
 931 the ring array's resolution can be retained with only the 40 TXs used in the Charge  
 932 1 survey and 40 RXs per TX. This, which dramatically reduces the size of the ring  
 933 array survey as shown in Table 7. The complete data-based RX selection methodology  
 934 is outlined in Table 8.

935 With only 1,600 data, this subset of the ring array survey is slightly smaller than  
 936 the comprehensive single linear array survey but far better resolves the conductive  
 937 structures around the tunnel. Considering that the full ring array survey had 630  
 938 TXs and 353,430 data, our ability to use the outlined survey design methodologies to  
 939 winnow it down to a survey with only 40 TXs and 1,600 data without considerable  
 940 sacrifices in model resolution is remarkable. Compared to the full ring array survey, this  
 941 reduces the number of TXs by ~94% and the number of data by ~99.5%. This

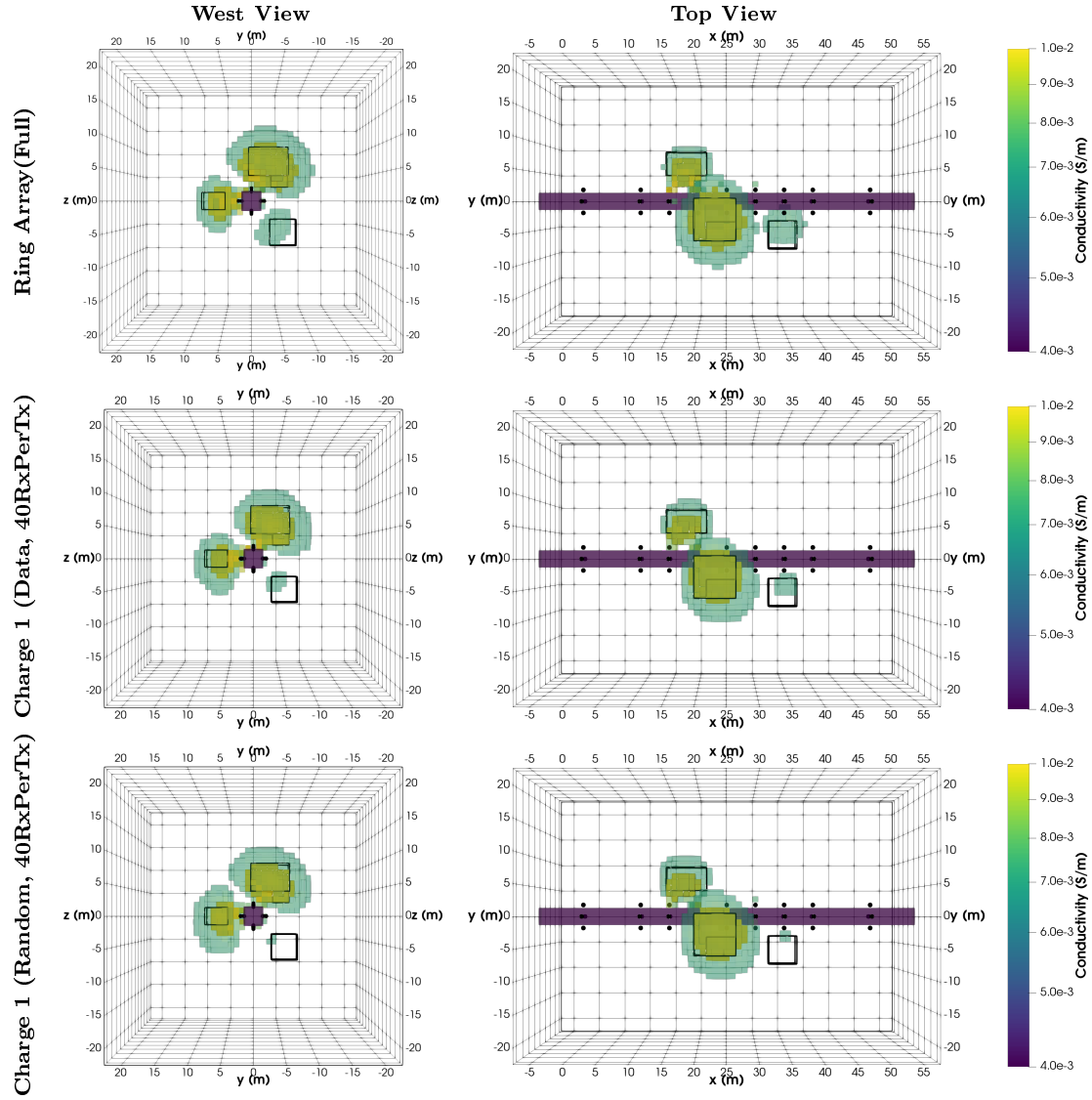


Figure 25: West and top views of volumetric cutoffs in the recovered models from the full ring array and both Charge 1, 40 RXs per TX surveys (data-based and purely random RX selection methods). These plots show that the data-based RX selection method better resolves block #3. Regions of high conductivity ( $\sigma \geq 0.01 \text{ S/m}$ ) are shown in yellow and regions of intermediate conductivity ( $\sigma \geq 0.007 \text{ S/m}$ ) in blue-green. The resistive tunnel is denoted by dark blue-purple cells, black outlines show the true location of the conductive blocks, and the black dots mark electrode locations.

Data Based RX Selection Methodology
<ol style="list-style-type: none"> <li>1. Define detectability thresholds (e.g., <math> \phi_t - \phi_p  =  \phi_s  \geq 1 \text{ mV}</math> and <math> \phi_s / \phi_p  \geq 0.1</math>.)</li> <li>2. For each selected TX form a subset of detectable RXs by identifying those RXs which had a detectable response to one or more of the test blocks used in the TX selection process.</li> <li>3. Bin the detectable RXs based on their MN offsets.</li> <li>4. Randomly select an equal number of RXs from each bin.</li> <li>5. If there are fewer RXs in a bin than the number required, randomly select RXs from other bins to ensure that each TX ends up with the specified number of RXs.</li> <li>6. Create a series of surveys with a progressively larger number of RXs per TX.</li> <li>7. For each survey forward model data using the synthetic model, add noise, and invert the data.</li> <li>8. Compare the inversion results of each survey using <math>\ \sigma_{inv} - \sigma_{true}\ _2</math> plots and visual differences to determine the point of diminishing returns (i.e., where the addition of more RXs has a minimal impact on resolution).</li> </ol>

Table 8: Workflow summarizing the steps in the data-based RX selection methodology.

942 removes—These reductions in survey size remove barriers associated with the huge  
 943 potential size of ring array surveys and makes them very manageable to collect.

944 **6. Discussion**

945 In this paper, we showed that when working in tunnels or other subterranean  
 946 environments the ring array can be effectively used to improve resolution and reduce  
 947 the non-uniqueness of recovered conductivity models when compared to conventional  
 948 single linear array surveys. Although single linear array surveys are often able to  
 949 identify the along-tunnel location of a target they cannot constrain its location around  
 950 the tunnel. With straight tunnel sections, the recovered anomaly is typically smeared  
 951 around the tunnel to form a characteristic ring-like shape. This ring-shaped anomaly  
 952 results from ambiguous measurements, which are due to the radial symmetry of the  
 953 problem, and an asymmetric distribution of sensitivities. This non-uniqueness in  
 954 the around-tunnel location of the anomaly can be alleviated through the use of ring  
 955 array surveys. The use of electrodes in all faces of the tunnel in the ring array survey  
 956 promotes the flow of primary currents around the tunnel to excite targets on all sides,  
 957 measures off-line potential differences, and creates a more symmetric distribution of  
 958 sensitivity around the tunnel. This greatly enhances resolution and allows All of  
 959 these factors enhance resolution and allow the ring array survey to better constrain  
 960 a target's location and shape.—This—which is especially important when trying  
 961 to accurately resolve more complex structures such as the multiple block model or  
 962 synthetic Mosaic model.

963 With more complex tunnel geometries that incorporate cross-tunnel measure-  
 964 ments, the ring array allows us to determine the location of the anomaly relative  
 965 to the plane of the tunnels. The asymmetric horseshoe shaped tunnel example in  
 966 Section 4.2.1 shows that the ring array can differentiate between targets which are

967 above and below the plane of the tunnels. With the linear array surveys, the re-  
968 covered anomaly remains pinned to the central plane of the tunnels regardless of its  
969 true  $z$ -location (see Mitchell (2020) for further analysis). An additional benefit of the  
970 ring array in this situation is that it can resolve anomalies on any side of the tunnel  
971 while the single linear array is primarily sensitive to structures in the central region  
972 between the tunnels.

973 Although existing infrastructure, such as tunnel branches and boreholes, should be  
974 utilized to place electrodes on different planes, reconnaissance surveying and forward  
975 modeling should be conducted before drilling additional boreholes. This additional  
976 analysis ensures that the benefits of a series of boreholes offset the cost. In the salt  
977 mine example, reconnaissance surveying is also a safety precaution that helps you  
978 avoid drilling into the water-bearing regions ~~that you are trying to image which are~~  
979 the targets of the geophysical imaging.

980 The benefits of the ring array come with one primary drawback.—A: a huge  
981 increase in the number of possible dipole-dipole measurements to collect. The physics-  
982 based survey design methodology presented here shows a simple and effective way to  
983 select a subset of ring array measurements that strike a balance between maximizing  
984 model resolution and minimizing survey size. The full survey design methodology is  
985 outlined in Table 9.

986 The trials presented here, with the multiple block model, show that most of the  
987 ring array's improved resolution can be gleaned with only a small subset including  
988 approximately 6% of the possible TXs and 0.5% of the RXs. This massive reduction  
989 in survey size results in a ring array survey which is slightly smaller than the compre-  
990 hensive single linear array, but has comparable resolution to the full ring array. In  
991 future work, it would be interesting to complete a comprehensive comparison of this  
992 survey design methodology with strictly optimal methods that make use of the model  
993 resolution matrix. This comparison would allow us to better quantify the differences  
994 in computational expense and model resolution.

995 The magnitude of this reduction in survey size is put into perspective by consid-  
996 ering how long it would take to collect each dataset. As discussed in Section 5, the  
997 IRIS Syscal Pro Switch system can collect a programmed sequence of ~30,000 mea-  
998 surements each day. The small survey analyzed here with only 36 electrodes shows  
999 how the size and cost of the full ring array survey can quickly become prohibitively  
1000 large. Using this system the full/comprehensive ring array survey with 630 TXs and  
1001 353,430 RXs would require about 11.8 days to collect. Whereas the Charge 1 survey  
1002 with 40 TXs and 22,440 RXs would require 18 hours and the Charge 1, 40 RX Per  
1003 TX survey with 40 TXs and 1,600 RXs would only require 1.3 hrs to collect.

1004 Since the resulting surveys only require a few hours to 1.4 days to collect, it should  
1005 be possible to design economically feasible surveys as the number of electrodes is  
1006 increased. For example, a full ring array survey with 120 electrodes (30 rings, each  
1007 with 4 electrodes) would contain close to 40 million possible measurements and require  
1008 about 3.7 years to collect. Without completing the survey design process for this  
1009 larger array it is difficult to estimate how many of the measurements are required to  
1010 balance resolution and survey size. Assuming that between 0.5 and 5% of the possible  
1011 data are needed, the resulting survey would contain somewhere between 200,000 and

### Survey Design Methodology

1. Design a synthetic model that matches your tunnel geometry and simulates the type of target you want to image.
2. Define the region of interest (ROI) to encompass target regions.
3. Layout ring array electrode locations (see Section 4.1) and design comprehensive survey.
  - Use forward modeling to gauge the detectability of targets with different sizes and offsets.
  - Try to balance inter-ring and intra-ring separation distances.
4. Use the TX selection methodology to find a set of TXs which best excite the ROI (see Section 5.1).
  - (a) Choose test block parameters (block size, conductivity, and a grid of locations within ROI).
  - (b) Move test block through the ROI and forward model responses (fields and comprehensive dataset).
  - (c) For each TX compute the amount of accumulated secondary charge on the given test block and rank TXs accordingly.
  - (d) Incrementally build up a list of the best TXs for each block, starting with the single best TX, then the best 2 TXs, and so forth. Add symmetric sets of selected TXs to create a series of surveys with progressively more TXs.
  - (e) For each survey forward model data using the synthetic model, add noise, and invert the data.
  - (f) Compare the inversion results of each survey using  $\|\sigma_{inv} - \sigma_{true}\|_2$  plots and visual differences to determine the point of diminishing returns (i.e., where the addition of more TXs has a minimal impact on resolution).
5. If necessary use the data-based RX selection methodology to find a minimal subset of RXs which preserve model resolution (see Section 5.2).
  - (a) Define detectability thresholds (e.g.,  $|\phi_t - \phi_p| = |\phi_s| \geq 1$  mV and  $|\phi_s|/|\phi_p| \geq 0.1$ .)
  - (b) For each selected TX form a subset of detectable RXs by identifying those RXs which had a detectable response to one or more of the test blocks used in the TX selection process.
  - (c) Bin the detectable RXs based on their MN offsets.
  - (d) Randomly select an equal number of RXs from each bin.
  - (e) If there are fewer RXs in a bin than the number required, randomly select RXs from other bins to ensure that each TX ends up with the specified number of RXs.
  - (f) Create a series of surveys with a progressively larger number of RXs per TX.
  - (g) For each survey forward model data using the synthetic model, add noise, and invert the data.
  - (h) Compare the inversion results of each survey using  $\|\sigma_{inv} - \sigma_{true}\|_2$  plots and visual differences to determine the point of diminishing returns (i.e., where the addition of more RXs has a minimal impact on resolution).

Table 9: Workflow summarizing the steps in the full survey design methodology.

1012 2,000,000 measurements. ~~Since this large of a~~ Such a large survey would require 6.7  
1013 to 67 days to collect using the IRIS system. ~~Therefore~~, other survey options might  
1014 have to be considered. The use of a distributed array system, in which all of the  
1015 RX measurements for a given TX can be recorded simultaneously, could be a good  
1016 option. This would dramatically increase the speed of data collection since the IRIS  
1017 Syscal Pro Switch system is only able to record 10 RX measurements per current  
1018 injection cycle. ~~To avoid noise due to electrode polarization, charge buildups around~~  
1019 ~~current electrodes need to be given time to decay before those electrodes are used as~~  
1020 ~~potential electrodes (Dahlin, 2000; Merriam, 2005; Wilkinson et al., 2012).~~

1021 Although a straight tunnel example is presented here, this survey design methodo-  
1022 gy can also be used with more complex tunnel configurations, such as the horseshoe  
1023 shaped tunnel. The ROI would simply need to be expanded to include the region be-  
1024 tween the tunnels. No modifications to the design process are required, but the larger  
1025 ROI increases the number of test block locations and the amount of time needed  
1026 for forward modeling. Also, note that this survey design methodology is not limited  
1027 to situations in which the reference model and region of interest are homogeneous.  
1028 The test block could just as easily be moved through a region with layered units of  
1029 differing conductivity or other known conductivity structures. Although this survey  
1030 design methodology was developed for use in tunnel-based environments there is no  
1031 reason that it cannot be adapted for ~~3D~~ 3-D surface surveys as well. This methodolo-  
1032 gy can be easily adapted and scaled for use in a variety of applications and is less  
1033 computationally expensive than many optimal design methods which are based on  
1034 the model resolution matrix.

1035 In a continuation of our research, we also extended this survey design methodology  
1036 and used it to design grounded source, frequency domain electromagnetic (FDEM)  
1037 surveys. The results of this work show that the EM surveys can better constrain  
1038 the shape, location, and conductivity of structures in the synthetic models than com-  
1039 parable DC resistivity surveys (Mitchell, 2020). Although we were able to highlight  
1040 some of the pros and cons of using an EM survey in underground environments, many  
1041 opportunities for future research remain.

1042 With the ability to design an economical ring array survey it can be used as a  
1043 reconnaissance tool instead of a single linear array. In this context, the ring array  
1044 provides a much more accurate estimate of the around-tunnel location of targets and  
1045 ensures that targets on all sides of the tunnel are detected. Following the inversion of  
1046 the initial ring array dataset, additional rings can be added to reduce the inter-ring  
1047 spacing or off-tunnel boreholes can be added to the region around identified anomalies  
1048 to increase resolution as required.

1049 An added benefit of the large reduction in survey size is that it also makes it more  
1050 feasible to collect reciprocal measurements, which can be used to quality control mea-  
1051 surements and better estimate uncertainties. Coupled with the improved resolution of  
1052 the ring array ~~this further increases~~, reciprocal measurements would further increase  
1053 the accuracy and reliability of the inversion results.

1054 By improving the way tunnel-based surveys are designed, this research will help re-  
1055 searchers more accurately image the regions surrounding tunnels using DC resistivity  
1056 inversions. The importance of this research is reinforced by the premature closure of

1057 the K1 and K2 portions of the Mosiac potash mine near Esterhazy, ~~SK Saskatchewan~~,  
1058 in June of 2021, due to their inability to control brine inflow. ~~Hopefully the The~~ techniques  
1059 described in this study ~~can may~~ help the new multibillion-dollar K3 shaft and  
1060 ~~mine workings other mines~~ avoid a similar fate. In addition to helping mining  
1061 engineers better image water inflow sources in potash mines, these ideas and methods  
1062 are generalizable to many tunnel-based applications where there is a contrast in con-  
1063 ductivity between the target and host rock. ~~Applications Other applications~~ could  
1064 include identifying water/air-filled voids, mapping extensions of ore bodies, detecting  
1065 fractured zones, or monitoring the structural competency of the rock surrounding a  
1066 tunnel.

## 1067 7. Acknowledgments

1068 We would like to thank Dr. Michael Maxwell for discussions regarding the use of  
1069 ring arrays. Along with Dr. Oldenburg, he collected a DC ring arrays dataset at the  
1070 Laboratoire Souterrain à Bas Bruit (LSBB) in Rustrel, Vaucluse, France (Maxwell  
1071 et al., 2010), but conflicting records of the electrode locations made this dataset  
1072 difficult to analyze. Dr. Maxwell has also been involved with several studies that  
1073 successfully used ring arrays to characterize the rock surrounding a vertical mine  
1074 shaft (Eso et al., 2006b; Cisyk et al., 2014; Maxwell and Cisyk, 2016). His optimism  
1075 prompted us to further investigate the merits of ring array DC resistivity surveys.

1076 We would also like to thank the SimPEG development team, including: Rowan  
1077 Cockett, Seogi Kang, Lindsey Heagy, Thibaut Astic, Dominique Fournier, Joseph  
1078 Capriotti, and Devin Cowan, for all the work they have put into SimPEG over the  
1079 years. Our research would not have been possible without this open-source python  
1080 package.

1081 A final word of thanks to all of our wonderful lab-mates at the UBC-Geophysical  
1082 Inversion Facility. Particular thanks go out to Sarah Devries, Thibaut Astic, Lindsey  
1083 Heagy, Dominique Fournier, Devin Cowan, Seogi Kang, Guðni Rosenkjær, Rowan  
1084 Cockett, and Joseph Capriotti for their insightful discussions and assistance.

1085 ~~We greatly appreciate the thoughtful and constructive reviews provided by Dr.~~  
1086 ~~Jonathan Chambers (British Geological Survey), Dr. Trevor Irons (University of~~  
1087 ~~Utah), and two anonymous reviewers. Your recommendations helped us clarify and~~  
1088 ~~number of issues and improved this article. Thank you.~~

1089 ~~Any use of trade, firm, or product names is for descriptive purposes only and does~~  
1090 ~~not imply endorsement by the U.S. Government.~~

## 1091 References

- 1092 Arai, E., 1995. A resistivity tomography test survey in the Toyoha Mine, Hokkaido,  
1093 Japan. Exploration Geophysics 25, 45–50. doi:10.1071/EG995045.
- 1094 Aster, R.C., Borchers, B., Thurber, C.H., 2018. Parameter Estimation and Inverse  
1095 Problems. 3 ed., Academic Press, Oxford. doi:10.1016/C2015-0-02458-3.

- 1096 Cisyk, D.E., Maxwell, M., Eso, R.A., 2014. Characterization of a water inflow fracture  
1097 system into a concrete mine shaft using geophysical and geological information, in:  
1098 International Discrete Fracture Network Engineering Conference, Vancouver, BC.
- 1099 Cockett, R., Heagy, L.J., Oldenburg, D.W., 2016. Pixels and their neighbors: Finite  
1100 volume. *Leading Edge* 35, 703–706. doi:10.1190/tle35080703.1.
- 1101 Cockett, R., Kang, S., Heagy, L.J., Pidlisecky, A., Oldenburg, D.W., 2015. SIMPEG :  
1102 An open source framework for simulation and gradient based parameter estimation  
1103 in geophysical applications. *Computers and Geosciences* 85, 142–154. doi:10.1016/  
1104 j.cageo.2015.09.015.
- 1105 Curtis, A., 1999. Optimal design of focused experiments and surveys. *Geophysical  
1106 Journal International* 139, 205–215. doi:10.1046/j.1365-246X.1999.00947.x.
- 1107 Dahlin, T., 2000. Short note on electrode charge-up effects in DC resistivity data  
1108 acquisition using multi-electrode arrays. *Geophysical Prospecting* 48, 181–187.  
1109 doi:10.1046/j.1365-2478.2000.00172.x.
- 1110 Dahlin, T., Zhou, B., 2004. A numerical comparison of 2D resistivity imaging  
1111 with 10 electrode arrays. *Geophysical Prospecting* 52, 379–398. doi:10.1111/  
1112 j.1365-2478.2004.00423.x.
- 1113 Eso, R.A., Maxwell, M., Oldenburg, D.W., Unrau, J., 2006a. Delineation of Water  
1114 Inflow in an Underground Potash Mine With 3-D Electrical Resistivity Imaging, in:  
1115 SAGEEP 2006 meeting, Expanded Abstracts, Seattle, Washington. doi:10.4133/  
1116 1.2923658.
- 1117 Eso, R.A., Oldenburg, D.W., Maxwell, M., 2006b. 3D DC Resistivity Inversion in an  
1118 Active Mineshaft, in: 18th International Workshop on Electromagnetic Induction  
1119 in the Earth, El Vendrell, Spain.
- 1120 Eso, R.A., Oldenburg, D.W., Maxwell, M., 2006c. Application of 3D electrical re-  
1121 sistivity imaging in an underground potash mine, in: SEG Technical Program Ex-  
1122 panded Abstracts, Society of Exploration Geophysicists, New Orleans. pp. 629–632.  
1123 doi:10.1190/1.2370339.
- 1124 Gibert, D., Nicollin, F., Kergosien, B., Bossart, P., Nussbaum, C., Grislin-Mouëzy,  
1125 A., Conil, F., Hoteit, N., 2006. Electrical tomography monitoring of the excavation  
1126 damaged zone of the Gallery 04 in the Mont Terri rock laboratory: Field ex-  
1127 periments, modelling, and relationship with structural geology. *Applied Clay Science*  
1128 33, 21–34. doi:10.1016/j.clay.2006.03.008.
- 1129 Haber, E., 2014. Computational Methods in Geophysical Electromagnetics. SIAM,  
1130 Philadelphia, PA. doi:10.1137/1.9781611973808.
- 1131 Haber, E., Ascher, U.M., Aruliah, D.A., Oldenburg, D.W., 2000. Fast Simulation of  
1132 3D Electromagnetic Problems Using Potentials. *Journal of Computational Physics*  
1133 163, 150–171. doi:10.1006/jcph.2000.6545.

- 1134 Haber, E., Heldmann, S., 2007. An octree multigrid method for quasi-static Maxwell's  
1135 equations with highly discontinuous coefficients. *Journal of Computational Physics*  
1136 223, 783–796. doi:10.1016/j.jcp.2006.10.012.
- 1137 Haber, E., Holtham, E., Granek, J., Marchant, D., Oldenburg, D., Schwarzbach,  
1138 C., Shekhtman, R., 2012a. An adaptive mesh method for electromagnetic inverse  
1139 problems, in: SEG Technical Program Expanded Abstracts, Society of Exploration  
1140 Geophysicists, Las Vegas. pp. 1–6. doi:10.1190/segam2012-0828.1.
- 1141 Haber, E., Magnant, Z., Lucero, C., Tenorio, L., 2012b. Numerical meth-  
1142 ods for A-optimal designs with a sparsity constraint for ill-posed inverse prob-  
1143 lems. *Computational Optimization and Applications* 52, 293–314. doi:10.1007/  
1144 s10589-011-9404-4.
- 1145 Han, D., Shi, X., Li, D., 2011. Study on Anomaly Characteristics of In-Advance DC  
1146 Detection of Water-Accumulating Gob in Abandoned Mines. *Procedia Earth and*  
1147 *Planetary Science* 3, 217–223. doi:10.1016/j.proeps.2011.09.086.
- 1148 Kaputerko, A., Gribenko, A., Zhdanov, M.S., 2007. Sensitivity analysis of marine  
1149 CSEM surveys, in: SEG Technical Program Expanded Abstracts, SEG, San Anto-  
1150 nio. pp. 609–613. doi:10.1190/1.2792493.
- 1151 Kessels, W., Flentge, I., Kolditz, H., 1985. DC Geoelectric Sounding to Determine  
1152 Water Content in the Salt Mine ASSE (FRG). *Geophysical Prospecting* 33, 436–  
1153 446. doi:10.1111/j.1365-2478.1985.tb00444.x.
- 1154 Kruschwitz, S., Yaramanci, U., 2004. Detection and characterization of the disturbed  
1155 rock zone in claystone with the complex resistivity method. *Journal of Applied*  
1156 *Geophysics* 57, 63–79. doi:10.1016/j.jappgeo.2004.09.003.
- 1157 LaBrecque, D.J., Miletto, M., Daily, W., Ramirez, A., Owen, E., 1996. The effects of  
1158 noise on Occam's inversion of resistivity tomography data. *Geophysics* 61, 538–548.  
1159 doi:10.1190/1.1443980.
- 1160 Li, Y., Oldenburg, D.W., 1994. Inversion of 3-D DC resistivity data using an  
1161 approximate inverse mapping. *Geophysical Journal International* 116, 527–537.  
1162 doi:10.1111/j.1365-246X.1994.tb03277.x.
- 1163 Loke, M., Barker, R.D., 1996. Practical techniques for 3D resistivity surveys and  
1164 data inversion. *Geophysical Prospecting* 44, 499–523. doi:10.1111/j.1365-2478.  
1165 1996.tb00162.x.
- 1166 Loke, M., Chambers, J., Rucker, D., Kuras, O., Wilkinson, P., 2013. Recent devel-  
1167 opments in the direct-current geoelectrical imaging method. *Journal of Applied*  
1168 *Geophysics* 95, 135–156. doi:10.1016/j.jappgeo.2013.02.017.
- 1169 Loke, M.H., Wilkinson, P.B., Uhlemann, S.S., Chambers, J.E., Oxby, L.S., 2014. Computation of optimized arrays for 3-D electrical imaging surveys. *Geophysical*  
1170 *Journal International* 199, 1751–1764. doi:10.1093/gji/ggu357.

- 1172 Maurer, H., Curtis, A., Boerner, D.E., 2010. Recent advances in optimized geophysical  
1173 survey design. *Geophysics* 75, A177—A194. doi:10.1190/1.3484194.
- 1174 Maxwell, M., Cisyk, D.E., 2016. ERI: A Geophysical Method for Evaluating Rock  
1175 Porosity Behind Concrete Mine Shafts, in: CIM, Canadian Institute of Mining,  
1176 Metallurgy and Petroleum, Vancouver.
- 1177 Maxwell, M., Eso, R.A., Oldenburg, D.W., Vorst, D.V., Yedlin, M., Guglielmi, Y.,  
1178 Cappa, F., Gaffet, S., 2010. Characterization of the Vaucluse Karst Aquifer Using  
1179 Electrical Resistivity, in: Proceedings of i-DUST, Apt, France. doi:10.1190/1.  
1180 2370339.
- 1181 Maxwell, M., Unrau, J., Eso, R.A., Oldenburg, D.W., Song, L.P., 2005. Advancement  
1182 of 2D and 3D Electrical Resistivity techniques for underground applications in  
1183 a potash mine, in: International Symposium on Mine Planning and Equipment  
1184 Selection, Banff.
- 1185 McGillivray, P.R., Oldenburg, D., 1990. Methods for Calculating Frechet Derivatives  
1186 and Sensitivities for the Non-Linear Inverse Problem: a Comparative Study. *Geo-*  
1187 *physical Prospecting* 38, 499–524. doi:10.1111/j.1365-2478.1990.tb01859.x.
- 1188 Menke, W., 1984. *Geophysical Data Analysis: Discrete Inverse Theory*. Academic  
1189 Press. doi:10.1016/B978-0-12-490920-5.X5001-7.
- 1190 Merriam, J., 2005. Injection Electrode Overprinting. *Journal of Environmental and*  
1191 *Engineering Geophysics* 10, 365–370. doi:10.2113/JEEG10.4.365.
- 1192 Mitchell, M., Oldenburg, D., 2016a. A statistical data quality control methodology  
1193 for large, non-conventional DC resistivity datasets, in: SEG Technical Program  
1194 Expanded Abstracts 2016, Society of Exploration Geophysicists, Dallas. pp. 948–  
1195 953. doi:10.1190/segam2016-13845441.1.
- 1196 Mitchell, M.A., 2020. Methodologies for the use of Electrical and Electromagnetic  
1197 Methods in Complex, Subterranean Environments. PhD thesis. University of  
1198 British Columbia (Vancouver). doi:10.14288/1.0389821.
- 1199 Mitchell, M.A., Oldenburg, D.W., 2016b. Data quality control methodologies for  
1200 large, non-conventional DC resistivity datasets. *Journal of Applied Geophysics*  
1201 135, 163–182. doi:<http://dx.doi.org/10.1016/j.jappgeo.2016.09.018>.
- 1202 Okpoli, C.C., 2013. Sensitivity and Resolution Capacity of Electrode Configurations.  
1203 *International Journal of Geophysics* 2013. doi:10.1155/2013/608037.
- 1204 Oldenburg, D.W., Li, Y., 2005. Inversion for Applied Geophysics: A Tutorial,  
1205 in: D. K. Butler (Ed.), *Investigations in Geophysics*, No. 13: Near-Surface Geo-  
1206 physics. Society of Exploration Geophysicists. chapter 5, pp. 89–150. doi:10.1190/  
1207 1.9781560801719.ch5.

- 1208 Parker, R.L., 1994. Geophysical inverse theory. Princeton University Press, Princeton.  
1209 doi:10.1515/9780691206837.
- 1210 Pidlisecky, A., Haber, E., Knight, R., 2007. RESINVM3D: A 3D resistivity inversion  
1211 package. *Geophysics* 72, H1–H10. doi:10.1190/1.2402499.
- 1212 Ramirez, A., Daily, W., Binley, A., Labrecque, D., Roelant, D., 1996. Detection of  
1213 Leaks in Underground Storage Tanks Using Electrical Resistance Methods. *Journal*  
1214 of Environmental and Engineering Geophysics
- 1215 1, 189–203. doi:10.4133/JEEG1.3. 189.
- 1216 Sasaki, Y., Matsuo, K., 1990. Surface-to-Tunnel Resistivity Tomography at a Copper  
1217 Mine, in: SEG Technical Program Expanded Abstracts, Society of Exploration  
1218 Geophysicists, San Francisco. pp. 550–553. doi:10.1190/1.1890260.
- 1219 van Schoor, M., 2005. The application of in-mine electrical resistance tomography  
1220 (ERT) for mapping potholes and other disruptive features ahead of mining. *The*  
1221 *Journal of The South African Institute of Mining and Metallurgy* 105, 447–452.
- 1222 van Schoor, M., Binley, A., 2010. In-mine (tunnel-to-tunnel) electrical resistance  
1223 tomography in South African platinum mines. *Near Surface Geophysics* 8, 563–  
1224 574. doi:10.3997/1873-0604.2010021.
- 1225 Scott, J.H., Lee, R.D., Carroll, D., Robinson, C.S., 1968. The relationship of geo-  
1226 physical measurements to engineering and construction parameters in the Straight  
1227 Creek Tunnel pilot bore, Colorado. *International Journal of Rock Mechanics and*  
1228 *Mining Sciences* 5, 1–30. doi:10.1016/0148-9062(68)90020-X.
- 1229 Spitzer, K., 1998. The three-dimensional DC sensitivity for surface and subsur-  
1230 face sources. *Geophysical Journal International* 134, 736–746. doi:10.1046/j.  
1231 1365-246X.1998.00592.x.
- 1232 Stummer, P., Maurer, H., Green, A.G., 2004. Experimental design: Electrical resis-  
1233 tivity data sets that provide optimum subsurface information. *Geophysics* 69, 120.  
1234 doi:10.1190/1.1649381.
- 1235 Tsourlos, P., Ogilvy, R., Papazachos, C., Meldrum, P., 2011. Measurement and inver-  
1236 sion schemes for single borehole-to-surface electrical resistivity tomography surveys.  
1237 *Journal of Geophysics and Engineering* 8, 487–497. doi:10.1088/1742-2132/8/4/  
1238 001.
- 1239 Uhlemann, S., Wilkinson, P., Maurer, H., Wagner, F., Johnson, T., Chambers, J.,  
1240 2018. Optimized survey design for electrical resistivity tomography: combined  
1241 optimization of measurement configuration and electrode placement. *Geophysical*  
1242 *Journal International* 214, 108–121. doi:10.1093/gji/ggy128.
- 1243 Wait, J.R., 1982. Geo-electromagnetism. Academic Press. doi:10.1016/  
1244 B978-0-12-730880-7.X5001-7.

- 1245 Wang, X., 2011. Technique of in-Advance Detection of Aquiferous Structures in the  
1246 Front of Excavation Working Face by Direct Current Electric Method. Procedia  
1247 Earth and Planetary Science 3, 66–75. doi:10.1016/j.proeps.2011.09.067.
- 1248 Wilkinson, P.B., Loke, M.H., Meldrum, P.I., Chambers, J.E., Kuras, O., Gunn,  
1249 D.A., Ogilvy, R.D., 2012. Practical aspects of applied optimized survey design for  
1250 electrical resistivity tomography. Geophysical Journal International 189, 428–440.  
1251 doi:10.1111/j.1365-246X.2012.05372.x.
- 1252 Wilkinson, P.B., Meldrum, P.I., Chambers, J.E., Kuras, O., Ogilvy, R.D., 2006. Im-  
1253 proved strategies for the automatic selection of optimized sets of electrical resistivity  
1254 tomography measurement configurations. Geophysical Journal International 167,  
1255 1119–1126. doi:10.1111/j.1365-246X.2006.03196.x.
- 1256 Yaramancı, U., 2000. Geoelectric exploration and monitoring in rock salt for the safety  
1257 assessment of underground waste disposal sites. Journal of Applied Geophysics 44,  
1258 181–196. doi:10.1016/S0926-9851(99)00013-0.